materials

MDPI

Article

Multi-Damage Localization in Plate-like Structures via Ultrasonic Guided Waves Based on a PSO-Optimized Elliptic Trajectory Algorithm

Shuxia Tian [1,*], Shunqiang Wang [1], Luyang Zhang [1], Zhiyong Li [1] and Yong Chang [2]

[1] Henan Provincial Key Laboratory of Intelligent Manufacturing of High-End Equipment, Zhengzhou University of Light Industry, Zhengzhou 450002, China; 142604010004@zzuli.edu.cn (S.W.); w2368124829@126.com (L.Z.); 17752531508@163.com (Z.L.)

[2] School of Mechanical and Electrical Engineering, Henan University of Technology, Zhengzhou 450001, China; changyong@haut.edu.cn

* Correspondence: tiansx@zzuli.edu.cn

Abstract

Plate-like structures serve as primary load-bearing components for industrial equipment, but multiple damage locations may coexist during service life. Conventional ultrasonic guided-wave elliptic trajectory localization depends on parameters chosen by experience, and its accuracy falls when multiple damages are present. This paper presents a particle swarm optimization (PSO) optimized elliptic trajectory method in which three parameters (the time-of-flight threshold, the equivalent group velocity and the damage factor) are calibrated once on a two-defect configuration and then held fixed during inspection. The healthy-state response of each specimen, recorded before its damage locations were introduced, supplies the template from which direct arrivals and cross-talk are removed, so no new healthy-state baseline is needed during subsequent inspections. The method is validated by finite-element simulations on Q235 steel plates and by experiments on the same plates and on woven carbon-fiber reinforced polymer (CFRP) laminates, each with two, three and four damage locations. The experimental mean normalized errors are 0.0146, 0.0237 and 0.0242 for steel and 0.0098, 0.0416 and 0.0251 for the laminate, each obtained with a separate calibration per material.

Keywords: structural health monitoring; plate-like structures; ultrasonic guided waves; elliptic trajectory algorithm; particle swarm optimization; multi-damage localization; CFRP composites

Check for updates

Academic Editor: Loic Hilliou

Received: 1 October 2026
Revised: 16 November 2026
Accepted: 23 November 2026
Published: 27 November 2026

Copyright: © 2026 by the authors. Licensee MDPI, Basel, Switzerland. This article is an open access article distributed under the terms and conditions of the Creative Commons Attribution (CC BY) license.

1. Introduction

Plate-like structures are fundamental load-bearing components in aerospace vehicles, rail transit car bodies, ship decks, pressure vessels, and wind turbine blades. Under long-term service in complex environments involving cyclic loading, corrosion, and impact, these structures are prone to multiple sites of concurrent damage, such as cracks, holes, delamination, and corrosion, which accelerate structural degradation and may trigger catastrophic failures [1]. Therefore, early and accurate multi-damage localization is a critical requirement for structural health monitoring (SHM) in industrial infrastructure.

Ultrasonic guided-wave technology has been established as a robust and effective SHM tool for plate-like structures due to its advantages of large-area coverage, long propagation distance, and high sensitivity to internal defects. The general rationale for structural health

monitoring is set out by Farrar and Worden [2], and the non-destructive techniques applied to composite pressure vessels are reviewed by Aramburu et al. [3]. In guided wave-based damage localization, several algorithms have been developed, including beamforming, time reversal, elliptic imaging, and probabilistic imaging methods [1,4]. Yan et al. [5] proposed a plate structure damage imaging method based on piezoelectric Lamb waves and the near-field MUSIC algorithm, realizing precise damage localization via signal mode separation and damage factor construction. Liu et al. [6] introduced a multi-frequency instantaneous wavenumber damage imaging method using laser-induced ultrasonic guided waves, achieving quantitative detection of defects with variable thickness through data fusion of multi-frequency wavenumber information.

Among various localization algorithms, the elliptic trajectory method based on ToF is attractive for its intuitive geometric principle, and it has been applied to multi-damage localization in plate-like structures [7]. In this method, each actuator–sensor pair defines an ellipse whose foci are the sensor locations, and the intersection of multiple ellipses indicates the damage position. However, the conventional elliptic trajectory algorithm suffers from two major limitations. First, its core parameters, including the ToF extraction threshold, equivalent group velocity, and damage factor, are manually determined based on empirical experience, introducing subjectivity and reducing adaptability to varying structural conditions. Second, in multi-damage scenarios, overlapping ellipses generate numerous false intersections, leading to severe artifacts, missed detections, and localization drift.

To overcome the above-mentioned limitations of parameter dependency and poor multi-damage performance, intelligent optimization algorithms have been introduced to guided wave-based damage localization. PSO, as a classical swarm intelligence algorithm, offers fast convergence, few adjustable parameters, and strong robustness, making it suitable for global parameter optimization. The algorithm was introduced by Kennedy and Eberhart [8], and the inertia-weight variant that improves its convergence was proposed by Shi and Eberhart [9]. Lomazzi et al. [10] examined to what extent convolutional networks processing ultrasonic guided-wave signals can be interpreted when they are used for damage diagnosis. Liu et al. [11] proposed an improved probability-based diagnostic imaging algorithm by correcting the weight distribution function with relative distances from defects to actuator–sensor pairs, effectively enhancing the damage localization accuracy for stiffened composite panels. However, existing PSO-based studies have primarily focused on single-defect localization in isotropic materials, with limited investigation into multi-damage scenarios in anisotropic composite structures.

In practical applications, plate-like structures often suffer from multiple defects during long-term service, with their interaction aggravating structural degradation. Compared with single-defect guided-wave detection, multi-damage detection involves more complex signals and greater imaging challenges. Liu et al. [12] proposed a damage monitoring method for plate-like structures using a compact rectangular phased piezoelectric transducer array, correctly identifying multi-hole defects via the total focusing method and sign coherence factor algorithms. Jin et al. [13] proposed a modified probabilistic damage imaging algorithm fusing time-domain and frequency-domain signal difference coefficients, though it has high signal quality requirements. Su et al. [14] proposed a damage localization imaging algorithm based on power spectral density and tomography, using the damage factor of power spectral density to locate single and double defects in strong noise environments. Chen et al. [15] addressed ToF deviation-induced defect localization inaccuracy, proposing the ellipse of uncertainty algorithm to weaken deviation interference. Tabjula et al. [16] proposed a statistical method based on outlier analysis, achieving delamination defect detection of composites at a 5 dB signal-to-noise ratio with less than 1% of traditional sampling points. Xu et al. [17] proposed a parameter estimation-based sparse

representation method for multi-modal Lamb wave separation and dispersion compensation. Kannusamy et al. [18] proposed the refined time-reversal method, combining optimal reconstruction frequency and extended wave packets to improve localization accuracy, and further proposed the virtual refined time-reversal method [19] to solve traditional virtual time-reversal localization failure. Xu et al. [20] proposed the relative amplitude variation coefficient as a new damage index, combining it with a probabilistic imaging algorithm to realize multi-damage localization. Yuan et al. [21] proposed a phased array focusing method for damage localization in curved plates. Its wave focusing and damage identification performance was verified via finite element simulations and curved aluminum plate tests, showing potential for real-time structural monitoring.

Notably, fiber-reinforced polymer composites are increasingly used in aerospace, new energy equipment, and hydrogen storage vessels due to their high specific strength and corrosion resistance. Unlike homogeneous metals, composites exhibit significant anisotropy and heterogeneity, causing guided waves to propagate with direction-dependent velocity, severe dispersion, and complex multimode coupling. The implementation strategies for guided-wave inspection of composites are reviewed by Ricci et al. [22], and the identification of damage in composite structures is reviewed by Su et al. [23]. These characteristics further exacerbate the limitations of conventional elliptic trajectory algorithms, which assume isotropic wave propagation. Thus, a parameter-adaptive localization method capable of handling both isotropic and anisotropic plate-like structures is urgently needed. Data-driven methods that learn this mapping directly from measured signals have been proposed as an alternative for composite structures. Deep networks have been trained on raw guided-wave signals to detect damage, assess its severity and regress its position [24]; the signals have also been re-encoded as images, for example, with Gramian angular fields [25] or as scalograms, and processed by convolutional networks: the explainability of such networks for guided-wave diagnosis is analyzed by Lomazzi et al. [10], and model-assisted convolutional and recurrent networks are used by Rautela and Gopalakrishnan [26]. Convolutional and recurrent architectures have been compared for guided-wave damage detection and localization in plate-like structures [26], and reviews of deep learning in structural health monitoring are available [27]. These methods reach high accuracy when a labelled dataset covering the damage scenarios of interest is at hand, but they learn the signal-to-position mapping from data and do not by themselves supply a physical criterion for separating several simultaneous defects, which is the situation addressed in this paper.

In this paper, a PSO-optimized elliptic trajectory algorithm is proposed for multi-damage localization in plate-like structures. The PSO algorithm is employed to adaptively optimize three key parameters: the ToF extraction threshold coefficient κ, the damage factor τ_0, and the Lamb wave group velocity C_g, using the reciprocal of the sum of Euclidean distances between predicted and actual damage positions as the fitness function. Compared with existing methods, the proposed approach exhibits three distinct novelties. First, it removes the need for a fresh baseline at every inspection: the healthy-state response of the structure is recorded once, before the damage is introduced, and is reused, together with the parameters calibrated from it, for all subsequent inspections carried out under the same configuration, which is advantageous for in-service structures where a reference measurement at the time of inspection is impractical. The template remains valid as long as the monitoring configuration is unchanged: the same transducer array, the same bonding condition and a comparable operating environment. Second, it integrates PSO into the traditional elliptic trajectory framework to overcome localization errors caused by manual empirical parameter selection. Simulation and experimental verifications are carried out on homogeneous Q235 steel plates, and the applicability of the proposed method to anisotropic CFRP laminates is also validated. The results show that the proposed method achieves

lower localization error under all working conditions compared with traditional algorithms. For a given material, the set of parameters calibrated under the double-damage condition can be directly adopted for cases with more damage sites without re-tuning.

2. Research Methods

2.1. Dispersion Curve Plotting and Excitation Signal Selection

Dispersion curves are an important basis for ultrasonic guided-wave testing, through which the variation laws of the wave velocity of each guided-wave mode with a frequency or frequency–thickness product can be clearly understood, including the group velocity C_g and phase velocity C_p. Group velocity refers to the overall propagation velocity of the wave packet, while phase velocity is the propagation velocity of the wave at a specific phase. In ultrasonic guided-wave testing, the group velocity dispersion curve is of particular concern because it directly determines the conversion relationship between ToF and propagation distance.

The plate-like structures investigated in this paper cover two typical material types: homogeneous isotropic Q235 steel plates and CFRP laminates. The wave propagation characteristics of these two materials differ fundamentally, thus requiring separate dispersion curve analyses to guide the selection of excitation signals.

2.1.1. Dispersion Curves of Q235 Steel Plates

Using the open-source software Dispersion Calculator, the group velocity and phase velocity dispersion curves of a 6 mm-thick Q235 steel plate were plotted, as shown in Figure 1a,b. The material parameters of Q235 steel are listed in Table 1.

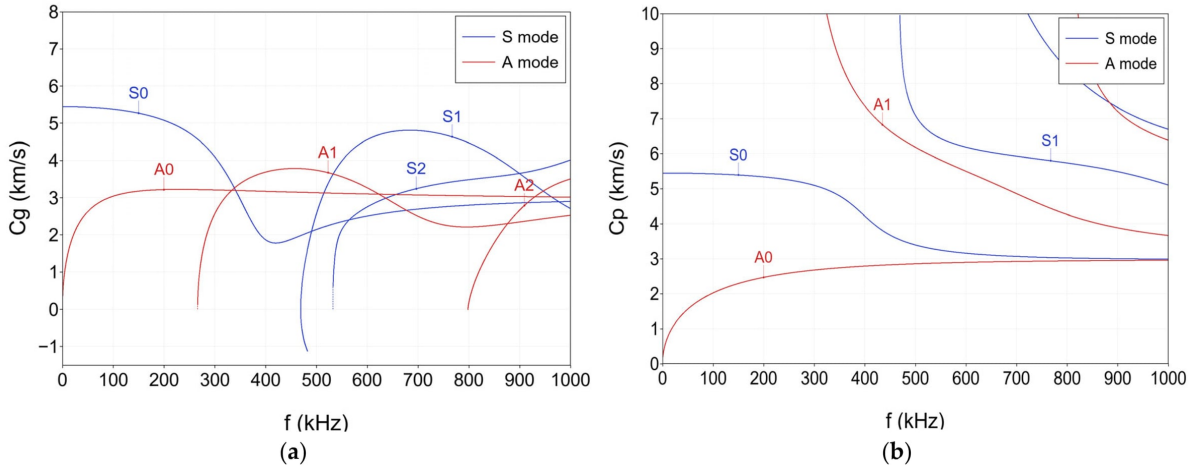


Figure 1. (**a**) Group velocity dispersion curves. (**b**) Phase velocity dispersion curves.

Table 1. Q235 material parameters.

Item	Density/(kg/m^3)	Elastic Modulus/GPa	Poisson's Ratio
Value	7850	200	0.3

2.1.2. Dispersion Curves of CFRP Laminates

The CFRP specimens are orthogonally woven 3K T700 carbon-fiber laminates with a total thickness of 5 mm. Because the two in-plane directions of an orthogonally woven fabric are equivalent, the woven plies are treated as one balanced orthotropic medium with the properties listed in Table 2, and the curves used to select the excitation frequency are computed for this medium; the same properties are used for all experimental results

reported below. Figure 2a,b give the group and phase velocity dispersion curves. They are computed along the 0° reference axis; the 0° and 90° curves coincide, and the 45° direction, where the deviation is largest, is included as the dashed curve. S0 falls from 6.9 km/s at 0° to 4.0 km/s at 45°, whereas A0 stays near 1.7 km/s in both directions because its high-frequency limit is set by the out-of-plane shear modulus, not by the in-plane stiffness. Each higher-order branch is traced from the frequency at which its phase velocity reaches the solver limit, marginally above the cut-off; the dotted segment opening such a branch marks the asymptotic approach to the cut-off, where the group velocity tends to zero and the phase velocity diverges, and is not a computed value. Group velocities are plotted with their sign, so the negative interval of the S1 branch of the steel plate just above its cut-off remains visible in Figure 1a. The constants in Table 2 are effective properties of the balanced woven medium, uncertain by a few percent, the usual spread for the elastic constants of a woven composite, and serve only to select the excitation frequency: a variation of several percent shifts the branches by less than the line width and leaves the band in which the two fundamental modes are best separated, and hence the 150 kHz choice, unchanged. Density is nominal, and the thickness of each specimen is measured.

Table 2. Properties of the orthogonally woven carbon-fiber laminate.

Item	Density/(kg/m^3)	E_1/GPa	E_2/GPa	E_3/GPa	G_{12}/GPa	G_{13}/GPa	G_{23}/GPa	ν_{12}	ν_{13}	ν_{23}
Value	1500	64	64	20	4.2	4.2	4.2	0.32	0.064	0.064

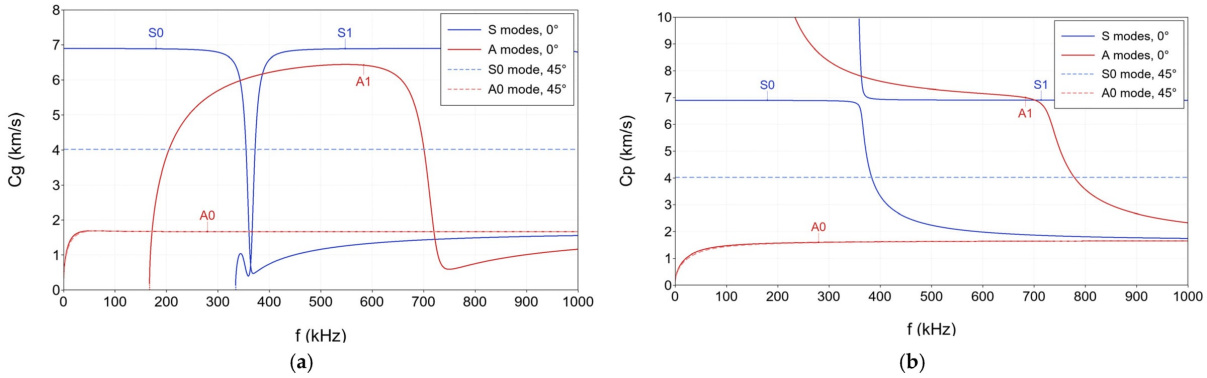


Figure 2. (**a**) Group velocity dispersion curves for the 0° (solid) and 45° (dashed) directions. (**b**) Phase velocity dispersion curves for the 0° (solid) and 45° (dashed) directions.

Figures 1 and 2 show fewer Lamb-wave modes and flatter velocity curves for the Q235 plate than for the laminate. In contrast, due to material anisotropy in CFRP laminates, the dispersion curves are more complex, and the mode coupling is more severe. This is precisely the fundamental reason why conventional isotropic localization algorithms fail in composite structures. The coupling is identified from the measured waveforms themselves: after the first arrivals, the signal does not return to zero but continues to oscillate, so that the packets of the different modes overlap in time. The same anisotropy is reflected in Figure 2: with an in-plane shear modulus of only 4.2 GPa (Table 2), S0 loses much of its velocity along 45°, whereas the A0 limit is set by the out-of-plane shear modulus.

Comprehensively analyzing the dispersion curves of both material types, the working point is placed below the first higher-order cut-off of both: the A1 branch starts at about 270 kHz for the 6 mm steel plate and at about 170 kHz for the 5 mm laminate (Figures 1a and 2a), so below the first cut-off, only the two fundamental modes propagate, with flat group-velocity curves. To accommodate the propagation characteristics of both materials while maintaining consistent experimental conditions, a Hanning window-

modulated 5-cycle sinusoidal signal with a center frequency of 150 kHz is uniformly selected as the excitation signal. The excitation signal is expressed as

$$x(t) = 0.5 - 0.5cos\left(\frac{2\pi f_c t}{n}\right) \cdot sin\ (2\pi f_c t) \quad (1)$$

In the equation, f_c is the center frequency of the sinusoidal wave, and n is the number of cycles of the sinusoidal wave. The excitation signal is shown in Figure 3a, and its amplitude spectrum in Figure 3b. Two features of this waveform need justification. The Hanning envelope suppresses the side lobes of a rectangular burst, so the packet has a single dominant peak, and its threshold crossing is unambiguous. Five cycles are the compromise between bandwidth and duration, since fewer cycles widen the spectrum until the A0 and S0 packets begin to overlap, while more cycles lengthen the packet and bring it closer to the edge reflections that follow it. At 150 kHz, the two fundamental modes are separated by 36 μs over the 290 mm steel path and by more than 100 μs in the laminate (Figures 1 and 2), both comparable to or larger than the 33 μs duration of the burst, so the scattered packet remains resolvable in time.

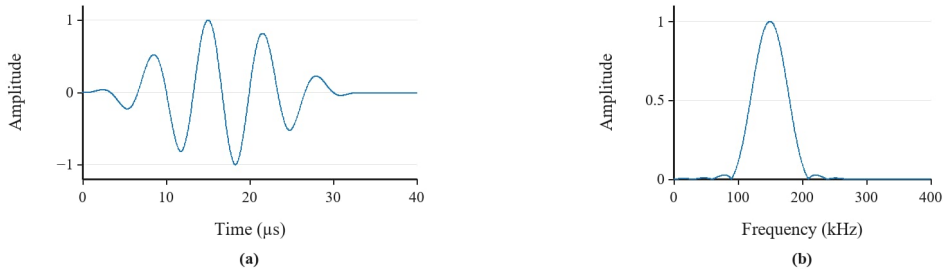


Figure 3. Excitation signal (**a**) and its amplitude spectrum (**b**).

2.2. Particle Swarm Optimization Algorithm

The PSO algorithm is a swarm intelligence optimization algorithm that simulates the foraging behavior of birds. Each particle has two attributes: velocity and position. It continuously adjusts its velocity and position according to the global best solution found by the particle swarm and the personal best solution found by the current particle to search for the optimal solution of the objective function [8]. The schematic diagram of particle update is shown in Figure 4:

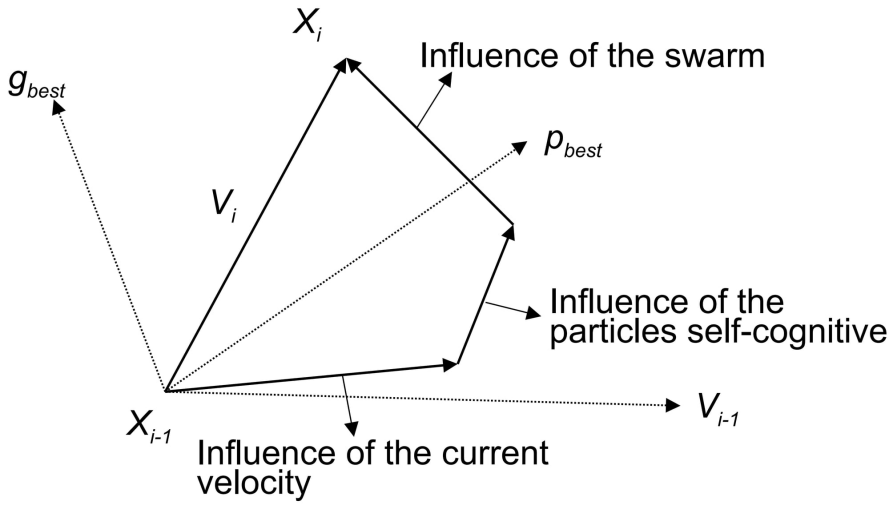


Figure 4. Particle update schematic diagram [28].

Suppose there are N particles in a population, where X_i represents the position of each particle at time i, V_i represents the velocity of each particle at time i, *pbest* denotes the optimal solution of the current particle in its search history, and *gbest* denotes the optimal solution of the entire particle swarm at the current moment. The choice of optimizer also needs justification. The search is only three-dimensional, and the objective is not differentiable: the ToF is obtained by thresholding an envelope, so the fitness changes in steps as κ moves from one sample to the next, and gradient-based methods do not apply. A grid search over the ranges used here would require more than 6000 evaluations, and a genetic algorithm would add crossover and mutation rates whose tuning is itself a search problem. PSO keeps a small population that shares the global best, reaches the optimum on this landscape within about 20 iterations (Section 3.2.1), and depends on two behavioral constants that were left at their standard values. The same optimizer was applied to the steel and to the CFRP case without retuning.

2.3. PSO-Optimized Elliptic Trajectory Algorithm with Pre-Experiment Calibration

2.3.1. Basic Principle of Elliptic Trajectory Imaging

The particle swarm optimization-based elliptic trajectory algorithm is developed on the basis of the traditional elliptic trajectory damage localization algorithm. It introduces the PSO algorithm to perform adaptive optimization of key parameters, solving the subjectivity and limitations of manually setting parameters in the traditional algorithm, thereby improving the localization accuracy of multiple damage sites in structures. The schematic diagram of its imaging principle is shown in Figure 5. Each coordinate point on the surface of the detected object can be regarded as a pixel point. In the figure, *P1* is the excitation sensor, *P2/P3/P4* are receiving sensors, (x, y) is the pixel point to be detected, where *Dak* and *Dsk* are the distances from the excitation sensor to the pixel point and from the pixel point to the receiving sensor, respectively. The difference from the traditional algorithm is that in this algorithm, the key parameters in the traditional process, such as the time-of-flight extraction threshold, damage factor τ_0, and group velocity C_g, are searched for the optimal values by the PSO algorithm instead of being manually set.

When P1 acts as the actuator and P3 as the receiver, if there is damage in the path, the guided wave will scatter. Sensor P3 receives the damage signal containing the scattered signal. After processing the scattered signal to obtain ToF, the damage location can be calculated by combining the group velocity C_g of Lamb waves in the plate. Compared with the traditional algorithm, the core difference is that the key parameters are optimized by the PSO algorithm before being substituted into the calculation. The specific process is as follows:

(1) Extraction of Scattered Signal and ToF

The scattered signal received by P3 was processed, but the extraction threshold of ToF is no longer set manually. Taking the "threshold coefficient κ" as one of the parameters to be optimized by the PSO algorithm, the optimal κ is searched by the PSO algorithm to ensure the accuracy of ToF extraction. The coefficient is defined on the Hilbert envelope of the scattered packet: if the envelope reaches its maximum A at time t_p, the arrival time is taken as the instant t_κ at which the leading edge first crosses κA, with $0 < \kappa \leq 1$. Figure 6 shows two values of κ: the lower threshold κA gives the instant t_κ, and the higher threshold κ'A gives the later instant t_κ'. Section 3.2.2 shows one such processed packet. A small κ places t_κ far on the leading tail, where the envelope is shallow and the crossing is easily displaced by noise; a large κ places it close to the crest, where the arrival is well defined but is registered later than the physical onset of the packet. Neither extreme is correct a priori, because the arrival time that is consistent with the array geometry is the one for which the elliptic loci of the different paths intersect at a single point. That is the

reason why κ is searched by the PSO algorithm over the interval 1–50% instead of being fixed by experience; it is dimensionless, but the calibrated value depends on the material (Table 3), which is why each material system is calibrated separately. The damage-scattered signal is obtained as the difference between the current response of the path and the healthy-state response of the same path, the latter being acquired once on the structure before the damage is introduced. The direct S0 and A0 packets, the excitation cross-talk and the reflections from the plate edges are present in both records and cancel in the difference. The residual therefore contains only the field scattered by the damage and the noise of the two acquisitions; consequently, the overlap between the S0 and A0 modes does not affect the picking of the scattered arrival. This differential operation is the standard way of separating the scattered field from the direct arrivals, the boundary reflections and the electrical cross-talk: Michaels [29] applies it with an in situ array of distributed sensors, and Croxford et al. [30] build their temperature-compensation strategy on the same residual; the temperature sensitivity of such a template is well documented [31].

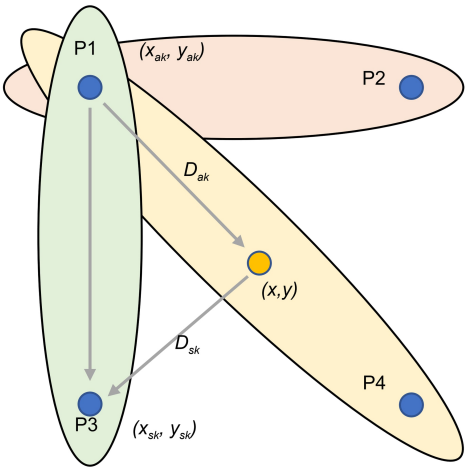


Figure 5. Elliptic trajectory algorithm principle schematic diagram.

Table 3. PSO settings and the calibrated parameter sets.

Parameter	Initial Values (Conventional)	Q235 (Simulation)	Q235 (Experiment)	CFRP (Experiment)
ToF threshold coefficient κ	50%	10%	10%	30%
Equivalent group velocity Cg (km/s)	3.00/2.05	3.10	2.88	1.91
Damage factor τ0	10	50	20	20

(2) Theoretical Calculation of Damage Location

Combined with the optimized Lamb wave group velocity C_g, the elliptic equation satisfied by the damage location still follows Equation (2), where C_g is the group velocity optimized by the PSO algorithm:

$$Dak + Dsk = \sqrt{(x - x_{ak})^2 + (y - y_{ak})^2} + \sqrt{(x - x_{sk})^2 + (y - y_{sk})^2} = ToF \cdot C_g^{opt} \quad (2)$$

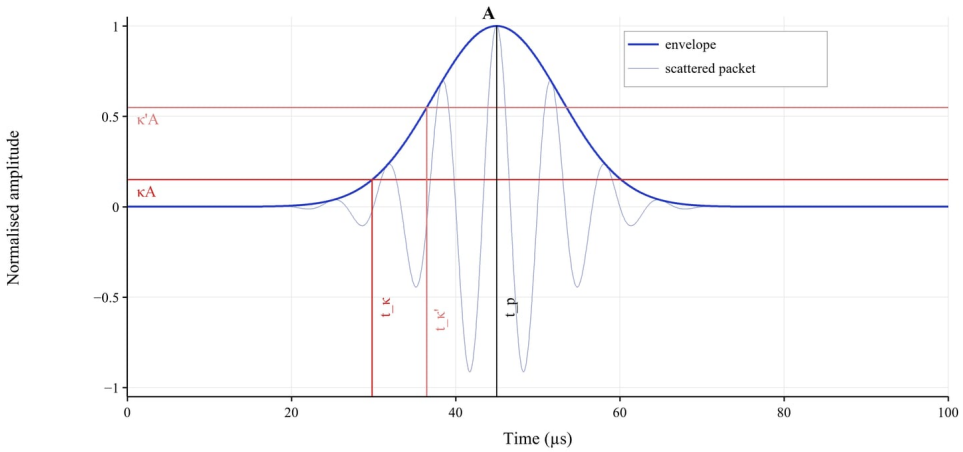


Figure 6. Threshold coefficient κ defined on the envelope of the scattered packet.

In the equation, *Dak* is the distance from the excitation sensor to the damage location in the k-th sensor path, *Dsk* is the distance from the damage location to the receiving sensor in the k-th sensor path, (x_{ak}, y_{ak}) and (x_{sk}, y_{sk}) respectively represent the coordinates of the excitation and receiving sensors in the *k*-th sensor path, and C_g^{opt} is the equivalent group velocity obtained by PSO optimization, i.e., a single value used for all sensing paths, which represents the propagation speed averaged over the array geometry rather than the physical group velocity of each individual path (Section 4.2). Because the time of flight is defined by the crossing of a fixed threshold on the leading edge of the packet, and not by the arrival of its envelope maximum, the velocity that maps this time onto the path length is an equivalent velocity rather than the group velocity read from the dispersion curve, and it may lie on either side of that value: it was below it for the steel plate and above it for the laminate. The difference depends on the threshold and on the amplitude of the scattered packet. The calibrated value is therefore an equivalent velocity consistent with the definition of the time of flight used in the imaging, and it is this internal consistency, rather than a close agreement with the tabulated group velocity, that the calibration establishes. When the scatterer lies on the segment joining the two transducers, the two distances add up to the focal distance, and the ellipse degenerates into that segment: the scattered packet then travels the same total distance as the direct arrival, is buried in it, and the path imposes no constraint along the line. The localization is therefore carried by the remaining paths, whose ellipses are non-degenerate. In the configurations examined in Section 3, each damage site lay on or close to one of the 28 paths; in the four-defect cases, two paths were degenerate, so that 26 to 28 non-degenerate ellipses contributed to a given localization.

(3) Damage Index and PSO Parameter Optimization

Each coordinate point on the surface of the detected object was regarded as a pixel point, and a damage index $p(x, y)$ is assigned to each pixel point (x, y). However, the damage factor τ_0 in the traditional algorithm is optimized to τ_0^{opt} by the PSO algorithm, and the damage index formula can be revised as

$$p(x,y) = \sum_{k=1}^{K} exp\left\{-\frac{\left|T_k^{TH}(x,y) - T_k^M\right|}{\tau_0^{opt}}\right\} \quad (3)$$

In the equation, k denotes the path index, K denotes the total number of paths, T_k^M is the value of parameter ToF obtained by processing the measured scattered signal; $T_k^{TH}(x,y)$ is the theoretical calculated ToF value based on the preset pixel point(x,y); and τ_0^{opt} is the damage factor obtained by PSO algorithm optimization. The color maps of the localization results in Section 3.2 and 3.3 display this damage index normalized by its maximum on

a 1 mm pixel grid, so that the plotted quantity is the same in every configuration. A parameter set that is inconsistent with the actual arrival times does not produce a point but a ridge: the elliptic loci fail to intersect in one place and the index remains elongated in the direction of the sensing paths. When the threshold coefficient, the equivalent group velocity and the damage factor are mutually consistent, the loci of the 28 paths cross within a small area, the index concentrates into a single peak, and the map appears compact and smooth after normalization by its maximum. This is why the maps of the optimized algorithm are smoother than those of the conventional one, which retains a ridge along the acquisition direction.

(4) Multi-Peak Extraction and Non-Maximum Suppression

The damage index of Equation (3) superposes the elliptic loci of all 28 paths, so that several damage sites produce several peaks together with spurious peaks generated by crossings of loci that belong to different defects. The field is normalized by its maximum, all local maxima on the pixel grid are collected, and the strongest is retained, while every maximum within a suppression radius R = 30 mm is discarded, the procedure being repeated on the remaining field. A retained peak is accepted as a defect if its normalized height exceeds a threshold α and is discarded otherwise, so that the number of defects is the number of accepted peaks and is not imposed a priori; α is not an optimization variable: in the calibration case, where the damage positions are known, a peak is labelled true when its position falls within 20 mm of a known defect and spurious otherwise, and α is defined as the midpoint between the tallest spurious and the weakest true peak; it is computed once from the calibration field and then held fixed for all subsequent cases. The same radius and threshold are applied to the conventional algorithm, so that the two algorithms are compared under identical detection rules. Both quantities are fixed by the geometry of the array and by the shape of the index peak, and neither was re-tuned for any of the cases reported below. The suppression radius must exceed the half-width of a single-defect peak. That half-width is set by the wavelength and by the array aperture (about 20 mm here), and the radius must stay below half the smallest separation between damage sites (70 mm here, so half is 35 mm); R = 30 mm satisfies both bounds with margin, and it scales with the array size rather than with the material or the damage condition. Because the index field is normalized by its maximum, the threshold α is dimensionless and separates true from spurious peaks by the same relative margin in every case. The identical values R = 30 mm and the α obtained from the calibration field were applied, without adjustment, to the two-, three- and four-defect configurations of both the steel and the CFRP specimens. This is the practical evidence that they are not reselected from structure to structure.

2.3.2. Basic Procedure of PSO Parameter Optimization

The core of the parameter optimization using the PSO algorithm is to search for the optimal values of the set of key parameters, namely the threshold coefficient κ, damage factor τ_0, and guided-wave group velocity C_g. The specific steps are as follows:

(1) Particle Encoding

The parameters to be optimized were encoded into particle dimensions, with each particle corresponding to a set of parameter combinations, an encoding also adopted for the quantitative damage detection of curved composite laminates [28].

$$X_i = \left[\kappa_i + \tau_{0i} + C_{gi}\right] \tag{4}$$

(2) Fitness Function

The parameter sets were evaluated by the reciprocal of the sum of Euclidean distances between the predicted damage positions and the actual damage positions, i.e.:

$$F(X_i) = \frac{1}{d_1 + d_2 + \varepsilon} \tag{5}$$

In the equation, X_i denotes the parameter combination corresponding to the i-th particle; d_1 and d_2 are the Euclidean distances between the predicted positions and actual positions of the two damage sites; ε is a small constant, introduced to avoid division by zero.

(3) Particle Iteration and Update

The velocity and position of each particle were updated under the guidance of the individual best $pbest_i$ and the global best $gbest$.

$$v_{ij}^{(t+1)} = \omega \cdot v_{ij}^{t} + c_1 \cdot r_1 \cdot \left(pbest_{ij} - X_{ij}^{t} \right) + c_2 \cdot r_2 \cdot \left(gbest_j - X_{ij}^{t} \right) \tag{6}$$

$$X_{ij}^{(t+1)} = X_{ij}^{t} + v_{ij}^{(t+1)} \tag{7}$$

In the equations, $v_{ij}^{(t+1)}$ and $X_{ij}^{(t+1)}$ are the velocity and position of the j-th dimension of the i-th particle at iteration t + 1, respectively; v_{ij}^{t} and X_{ij}^{t} are the velocity and position at iteration t; ω is the inertia weight; c_1 and c_2 are learning factors; r_1 and r_2 are random numbers uniformly distributed between 0 and 1; $pbest_{ij}$ is the j-th dimension of the individual best position of the i-th particle; and $gbest_j$ is the j-th dimension of the global best position of the particle swarm. The optimization was carried out with a particle swarm optimizer implemented in-house, with a swarm of 30 particles, on the search ranges κ = 1–50% (step 5%), $\tau 0$ = 10–100 (step 10) and Cg = 2700–3300 m/s for the steel plate and 1845–2255 m/s for the laminate, starting from the initial values given in Table 3. The inertia weight decreases linearly from 0.95 to 0.40 over the iterations, the cognitive coefficient decreases from 2.5 to 1.5, and the social coefficient increases from 1.5 to 2.5; the search was stopped after 50 iterations, or earlier when the best fitness changed by less than 1% over five consecutive iterations.

After the PSO iteration was completed, the parameter set obtained from the PSO run was substituted into Equations (2) and (3) to calculate the damage index $p(x,y)$ of each pixel point; the coordinate corresponding to the maximum damage index was the optimized predicted damage position, thereby improving the localization accuracy.

2.3.3. Parameter Calibration Mechanism Based on Pre-Experiment

To apply the aforementioned PSO parameter optimization method to practical engineering scenarios where damage information is unknown in advance, a pre-experiment calibration procedure is established. It is what connects the algorithm to on-site use.

(1) Engineering Application Value of Pre-experiment Calibration

In practical structural health monitoring, the location and number of damage positions are unknown during the detection stage, so the PSO algorithm with known damage positions cannot be directly used for real-time parameter optimization. The traditional manual parameter setting method relies heavily on empirical experience, resulting in poor adaptability to different structures and damage conditions. The pre-experiment calibration uses simulated scatterers rather than real damage to complete parameter tuning. In the experiments reported here, the laminate was calibrated with magnets bonded to both faces, whereas the steel plates were calibrated with through-thickness holes; a calibration based entirely on non-destructive scatterers has therefore been demonstrated for the laminate only. This leaves the structural integrity intact and meets the on-site requirement of in-service industrial structures. Once calibrated, the parameter set can be reused for subsequent inspections, provided that the structural and environmental conditions remain comparable.

This shortens the preparation time for each inspection. The temperature sensitivity of the template is the reason for this restriction: guided-wave baselines drift measurably with temperature and require compensation otherwise: Konstantinidis et al. [31] quantify the stability limit, and Croxford et al. [30] compare the strategies that restore it. The calibration follows a fixed procedure. The healthy response of every path is recorded first and stored as the template. Through-thickness holes in the steel plate and pairs of small magnets bonded symmetrically on both faces of the laminate are then introduced at two known positions, the 28 signals are recorded again, and the difference with the template yields the scattered packets from which the ToF is extracted. The PSO then searches κ, $\tau 0$ and Cg so that the elliptic loci of the paths intersect at the known positions, and the converged set is stored and reused. The procedure needs one acquisition per configuration, does not require the structure to be unloaded, and is repeated only when the template is renewed.

(2) Calibration logic of the parameter set

Typical simulated damage conditions are selected as the calibration benchmark. On the basis of the PSO parameter optimization process described in Section 2.3.2, the fitness function is revised to a general form applicable to any number of damage positions to meet the global calibration requirement:

$$F(X_i) = \frac{1}{\sum_{i=1}^{n} d_i + \varepsilon} \tag{8}$$

where n is the number of calibrated damage sites, d_i is the Euclidean distance between the predicted and actual position of the i-th damage site, and ε is a small constant to avoid division by zero. Different from scenario-by-scenario parameter optimization, the output of this calibration process is a single parameter set. The same set is applied to all multi-damage scenarios without matching the parameters to the number of damage site.

(3) Two-step workflow of calibration and detection

Pre-experiment calibration stage: Arrange the PZT array on the structure to be tested, set non-destructive simulated defects, collect guided-wave signals of all paths, and obtain the calibrated parameter set through PSO iterative optimization.

On-site detection stage: Directly substitute the calibrated global parameter set into the elliptic trajectory imaging formula to calculate the damage index of each pixel and output the damage localization results. No new baseline measurement and no prior damage information are required in this stage. The template is the healthy-state record of the structure being inspected, acquired before its damage was introduced; the parameter set is the one established during the calibration, and it is the parameter set rather than the template that is carried over between damage configurations. The calibration is carried out three times, once per domain, and no parameter set crosses the boundary between simulation and experiment. The set optimized on the simulated responses of the Q235 plate is used only for the simulated Q235 cases, the set optimized on the measured responses of the Q235 plates only for the Q235 experiments, and the set optimized on the measured responses of the CFRP laminates only for the CFRP experiments. Table 3 lists the PSO settings together with the three calibrated parameter sets, namely the one obtained from the simulated responses of the Q235 plate and the two obtained from the measured responses of the Q235 and CFRP specimens.

2.4. Localization Error Evaluation Criteria

To quantitatively assess the damage localization accuracy, four evaluation indicators are defined with the reference length $L = 290$ mm, i.e., the aperture of the sensor array (the distance between PZT1 and PZT5), and all results are retained to 4 decimal places. The calculation rules are as follows:

(1) X and Y coordinate localization error: Directly use the coordinate difference $(\Delta x, \Delta y)$ between the localized coordinates $(x_{\text{loc}}, y_{\text{loc}})$, and the preset damage coordinates $(x_{\text{pre}}, y_{\text{pre}})$, where

$$\begin{cases} \Delta x = x_{\text{loc}} - x_{\text{pre}} \\ \Delta y = y_{\text{loc}} - y_{\text{pre}} \end{cases} \tag{9}$$

(2) Relative distance: The Euclidean distance d between the localized point and the preset damage point (independent of L), calculated as

$$d = \sqrt{\Delta x^2 + \Delta y^2} \tag{10}$$

(3) Localization error ε_{loc}: Normalized by the reference length L, calculated as

$$\varepsilon_{\text{loc}} = \frac{d}{290} \tag{11}$$

(4) Mean localization error: $\varepsilon_{\text{loc}i}$ denotes the normalized localization error of the i-th damage, where n is the number of defects:

$$\overline{\varepsilon_{\text{loc}}} = \frac{1}{n}\sum_{i=1}^{n} \varepsilon_{\text{loc}i} \tag{12}$$

3. Numerical Simulation and Experimental Verification

To systematically verify the multi-damage localization performance and engineering applicability of the proposed algorithm, this chapter carried out validation on homogeneous Q235 steel plates via numerical simulations and experimental tests. Simultaneously, experimental verification was conducted on CRFP composite laminates. Three damage configurations with two, three and four simulated points of damage are set for both types of specimens (through-thickness holes in the models and magnets bonded to the surface in the CFRP experiment). The 2-defect configuration is used for pre-experiment parameter calibration to obtain the calibrated parameter set, while the 3-defect and 4-defect configurations serve as independent test sets for localization accuracy verification, and a horizontal comparison with the conventional unoptimized elliptic trajectory algorithm is conducted. The subsequent sections of this chapter will elaborate on the finite element model construction, experimental platform setup, pre-experiment calibration process, and multi-damage localization results.

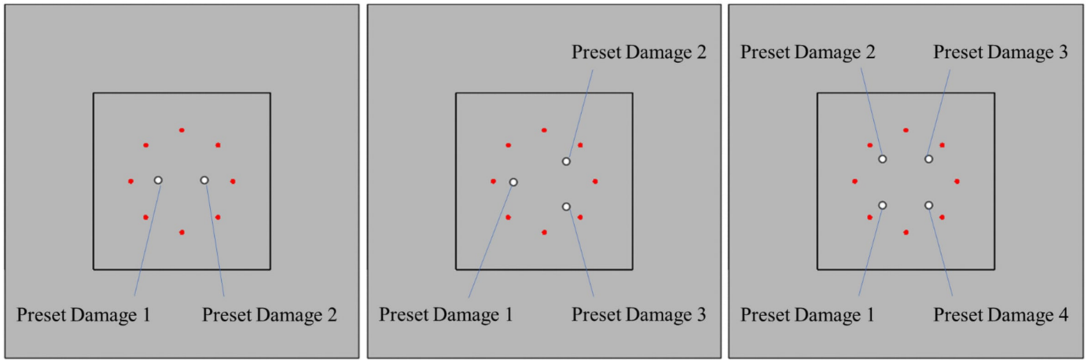
3.1. Damage Model and PZT Configuration

In this section, a finite element damage model of a Q235 homogeneous steel plate is established, and the PZT arrangement and the path planning used for both the simulations and the experiments are described. The same arrangement is adopted for the CFRP specimens, so that the two material systems can be compared on a common basis.

3.1.1. Q235 Steel Plate Damage Model

A three-dimensional finite element model of Q235 steel plates is established using ABAQUS/Explicit 2022, with dimensions of 1000 mm × 1000 mm × 6 mm. The material parameters are listed in Table 1. In the model, 2, 3, and 4 circular through-hole defects with a radius of 10 mm are preset, forming three damage conditions, as shown in Figure 7. The model adopts C3D8R elements with an edge length of 1 mm, i.e., about 21 elements per wavelength for the A0 mode at the excitation frequency, well above the ten-element-per-wavelength criterion recommended for guided-wave simulations: the spatial discretization

required for elastic wave propagation was established by Moser et al. [32], and the simulation methods available for guided-wave SHM are reviewed by Willberg et al. [33]. The model contains 6.0×10^6 C3D8R elements and 7.0×10^6 nodes, i.e., about 2.1×10^7 degrees of freedom, and is solved with ABAQUS/Explicit. The simulation time step is set to 1×10^{-8} s, and the total calculation time is 2×10^{-4} s, to ensure that all PZTs receive complete guided-wave signals.



(**a**) Two-defect simulation model (**b**) Three-defect simulation model (**c**) Four-defect simulation model

Figure 7. Finite element simulation models of Q235 steel plates with different damage conditions.

3.1.2. PZT Arrangement and Path Planning

The finite element model and both experimental specimens adopt an annular array composed of eight piezoelectric transducers (PZTs), each with a diameter of 8 mm and a thickness of 0.5 mm, uniformly arranged around the preset damage positions, as shown in Figure 8. In the finite element models, the transducers are not discretized as piezoelectric elements: the excitation of Equation (1) is applied as a prescribed out-of-plane displacement over the transducer footprint, and the response is recorded as the out-of-plane displacement at the receiving position. The prescribed displacement is used because the guided-wave field is governed by the spatial and temporal distribution of the motion that the wafer imposes on the substrate, rather than by the electrical response of the transducer. A bonded PZT driven in the d31 mode strains the substrate through the shear lag at the bond line, and over the 8 mm footprint, the resulting out-of-plane motion is well represented by a uniform displacement carrying the waveform of Equation (1). Discretizing the wafer as a piezoelectric solid would add the electrical boundary conditions and the adhesive layer to the model, but it would not change the time of flight or the scattering pattern on which the localization relies, and the transmitted waveform is in any case calibrated against the measured signal. The displacement amplitude is chosen so that the resulting A0 strain remains in the linear elastic range. This source model has been adopted for comparable guided-wave problems [34].

The guided-wave signals between any pair of PZTs exhibit strict acoustic reciprocity in plate-like structures [35]. For instance, the signal excited by PZT 1 and received by PZT 2 is nearly identical to that excited by PZT 2 and received by PZT 1 in terms of waveform, amplitude and time-of-flight. In accordance with the well-established paradigm in Lamb wave-based structural health monitoring [36], only one direction of each transducer pair is retained, which reduces the $8 \times 7 = 56$ ordered pairs to the 28 physical paths of the array. This reduction follows from the reciprocity of the medium and is decided before any measurement is taken: no path is discarded on account of the bonding quality of the transducers, and all eight PZTs are bonded and all 28 paths are used in the imaging. Detailed path information and PZT coordinates are presented in Table 4.

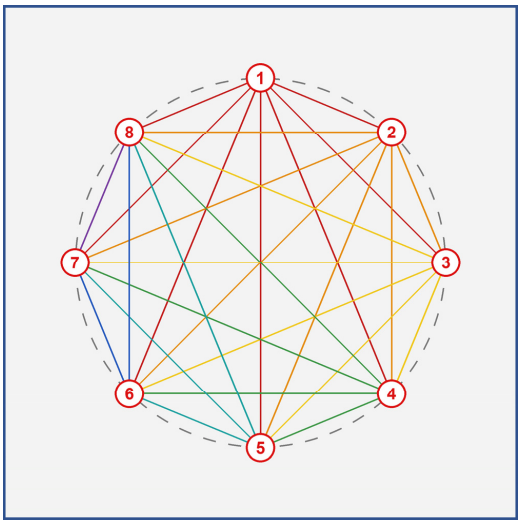


Figure 8. PZT arrangement diagram.

Table 4. The 28 guided-wave propagation paths and the PZT coordinates.

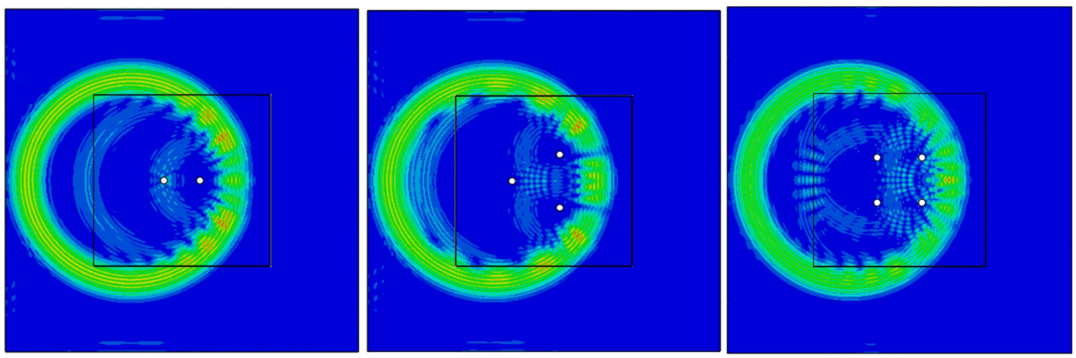
Excitation PZT	Receiving PZT	Number of Paths
1 (500, 645)	2/3/4/5/6/7/8	7
2 (397.5, 602.5)	3/4/5/6/7/8	6
3 (355, 500)	4/5/6/7/8	5
4 (397.5, 397.5)	5/6/7/8	4
5 (500, 355)	6/7/8	3
6 (602.5, 397.5)	7/8	2
7 (645, 500)	8 (602.5, 602.5)	1
Total Paths		28

3.2. Damage Localization on Q235 Steel Plates

This section focuses on Q235 homogeneous steel plates. The multi-damage localization performance of the PSO-optimized elliptic trajectory algorithm in homogeneous isotropic materials is verified through finite element simulations and experimental tests. The simulations and experiments adopt identical model dimensions, PZT arrangement, and excitation signal parameters, with damage conditions covering two, three, and four through-hole defects.

3.2.1. Numerical Simulation Verification

Figure 9 shows the simulation results of the ultrasonic Lamb wave propagation process in the plate. The wavefronts radiate from the excitation point and broaden as they travel outward. As the propagation distance increases, the wave packet broadens and its peak amplitude decreases, owing to dispersion and to the geometric spreading of the wave front: the dispersion that broadens the packet is treated by Rose [37], and the amplitude decay of a spreading wavefront in a plate is quantified by Giurgiutiu [38]. After the guided wave interacts with the defects, scattering and reflection phenomena occur.



(**a**) Two-defect model (**b**) Three-defect model (**c**) Four-defect model

Figure 9. Wavefield snapshots of the ultrasonic Lamb wave propagation in the different damage models.

(1) Simulation Verification of Two Defects

The numerical simulation model for two defects is shown in Figure 7a, and the simulated wavefield snapshot is shown in Figure 9a. The guided-wave signals of 28 paths were extracted, and the positioning was carried out using the elliptic trajectory algorithm and the PSO-based elliptic trajectory algorithm. The positioning results are shown in Figure 10.

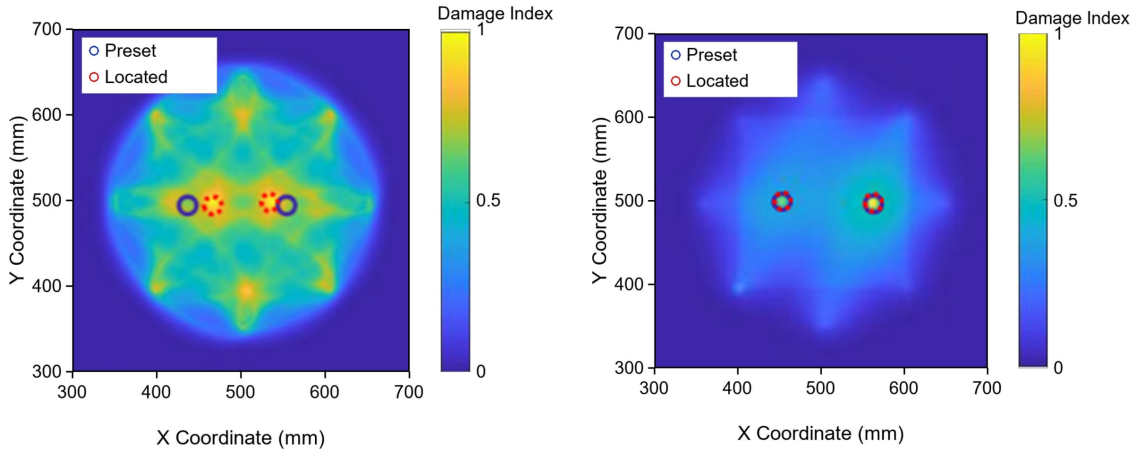


Figure 10. Two-defect simulation localization results. (**a**) Two-defect localization results of elliptic trajectory algorithm; (**b**) Two-defect localization results of PSO-based elliptic trajectory algorithm.

The two-defect case is taken as the benchmark condition for pre-experiment parameter calibration. Both the conventional elliptic trajectory algorithm with empirical parameters and the PSO-optimized elliptic trajectory algorithm are implemented for imaging in this case, to complete the parameter optimization process and compare the adaptation performance of different parameter schemes.

As shown by the localization results, both algorithms achieve relatively sound positioning performance in the Y direction, and the positioning errors mainly occur in the X direction. Compared with the empirical parameter set used in the conventional algorithm, the PSO-optimized parameter combination yields smaller positioning deviation under the calibration condition, demonstrating better parameter adaptability. The detailed positioning error values corresponding to the two parameter schemes are presented in Table 5. The calibrated parameter set obtained from this calibration will be applied to the independent verification of the following three-defect and four-defect scenarios.

Table 5. Two-defect simulation localization error table.

Algorithm Name	PSO-Based Elliptic Trajectory Algorithm	Elliptic Trajectory Algorithm
Preset Damage Coordinates	1.(450, 500), 2.(550, 500)	1.(450, 500), 2.(550, 500)
Algorithm-Localized Damage Coordinates	1.(448, 501), 2.(551, 503)	1.(470, 501), 2.(532, 502)
X and Y Coordinate Localization Error (mm)	1.(−2, 1), 2.(1, 3)	1.(20, 1), 2.(−18, 2)
Relative Distance (mm)	1.(2.24), 2.(3.16)	1.(20.03), 2.(18.11)
Localization Error ε_{loc}	1.(0.0077), 2.(0.0109)	1.(0.0691), 2.(0.0624)
Mean Error	0.0093	0.0658

To intuitively demonstrate the optimization process and convergence performance of the PSO algorithm during pre-experiment calibration, Figure 11 presents the typical convergence curve under the two-defect calibration case. The ordinate is the reciprocal of the fitness defined in Equation (5), so the plotted curve falls as the fitness rises. At the initial stage, the particles are randomly distributed with low fitness values. As iterations proceed, the particles gradually approach the optimal solution guided by the individual best and global best, and the fitness value rises rapidly. After approximately 20 generations, the fitness value stabilizes, indicating that the PSO calibration process converges to a stable parameter set. The optimal parameter set obtained from this calibration condition will be uniformly used for the subsequent independent verification of three-defect and four-defect scenarios.

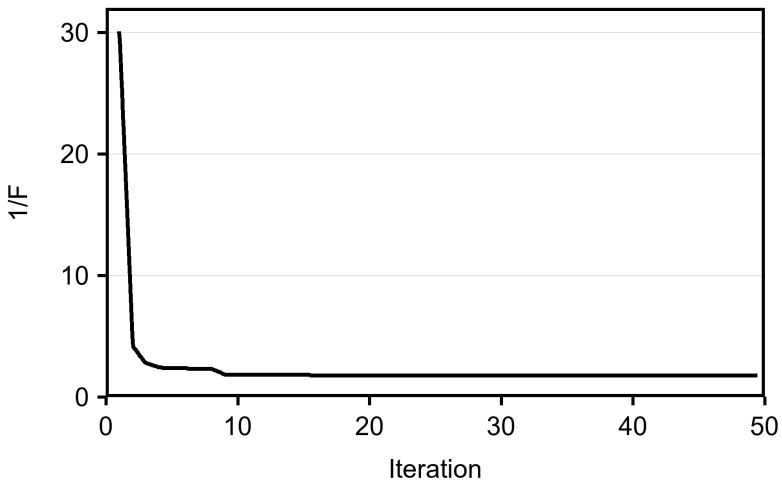


Figure 11. Typical convergence curve of the PSO algorithm for the two-defect case.

(2) Simulation Verification of Three Defects

The numerical simulation model for three defects is shown in Figure 7b, and the simulated wavefield snapshot is shown in Figure 9b. Figure 9b shows that the propagation law of ultrasonic guided waves in the structure is the same as that in the structure with two defects, but the scattering and reflection phenomena of the guided wave after interacting with the defects are more complex than those with two defects, which puts higher requirements on the positioning accuracy of the algorithm. Using the same processing method as the simulation results for the two-defect case, the guided-wave signals of 28 paths were extracted, respectively, and then the positioning was carried out using the elliptic

trajectory algorithm and the PSO-based elliptic trajectory algorithm. The positioning results are shown in Figure 12.

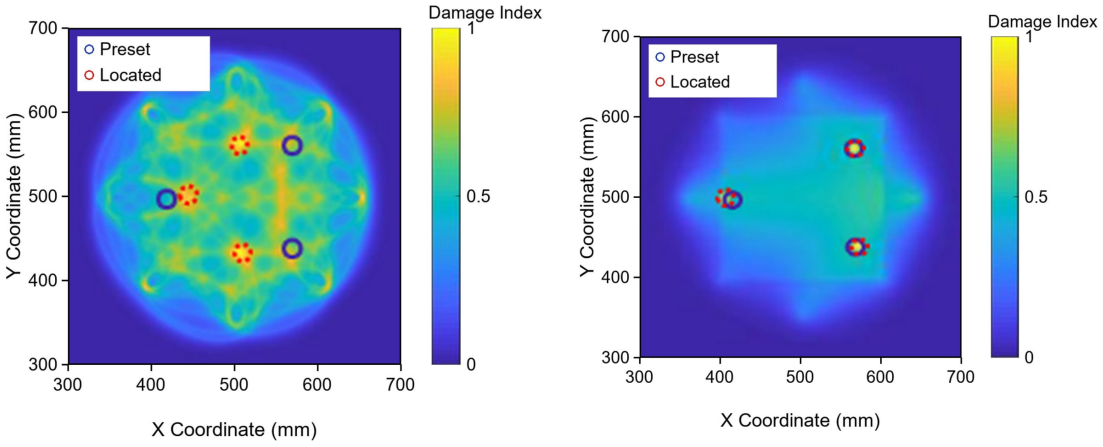


Figure 12. Three-defect simulation localization results. (**a**) Three-defect localization results of elliptic trajectory algorithm; (**b**) Three-defect localization results of PSO-based elliptic trajectory algorithm.

The three-defect localization results are shown in Figure 12. When the number of defects rises from two to three, the X-direction error of the elliptic trajectory algorithm grows further, whereas the PSO-based algorithm still locates all three. The mean error of the PSO-based algorithm in this configuration is 0.0114, against 0.1739 for the conventional one. The positioning errors of the two methods are shown in Table 6.

Table 6. Three-defect simulation localization error table.

Algorithm Name	PSO-Based Elliptic Trajectory Algorithm	Elliptic Trajectory Algorithm
Preset Damage Coordinates	1.(410, 500), 2.(545, 425), 3.(545, 575)	1.(410, 500), 2.(545, 425), 3.(545, 575)
Algorithm-Localized Damage Coordinates	1.(404, 501), 2.(548, 426.5), 3.(545, 575.5)	1.(419, 505), 2.(476, 423), 3.(473, 574)
X and Y Coordinate Localization Error (mm)	1.(−6, 1), 2.(3, 1.5), 3.(0, 0.5)	1.(9, 5), 2.(−69, −2), 3.(−72,−1)
Relative Distance (mm)	1.(6.08), 2.(3.35), 3.(0.5)	1.(10.30), 2.(69.03), 3.(72.01)
Localization Error ε_{loc}	1.(0.0210), 2.(0.0116), 3.(0.0017)	1.(0.0355), 2.(0.2380), 3.(0.2483)
Mean Error	0.0114	0.1739

(3) Simulation Verification of Four Damages

The simulation model for four defects is shown in Figure 7c, and the simulated wavefield snapshot is shown in Figure 9c. Figure 9c shows a more complex scattering pattern than the earlier snapshots, which places correspondingly higher demands on the localization accuracy. Using the same processing method as the simulation results for the two-defect

and three-defect cases, the guided-wave signals of 28 paths were extracted. The damage localization was performed using the above two methods, and the localization results are shown in Figure 13.

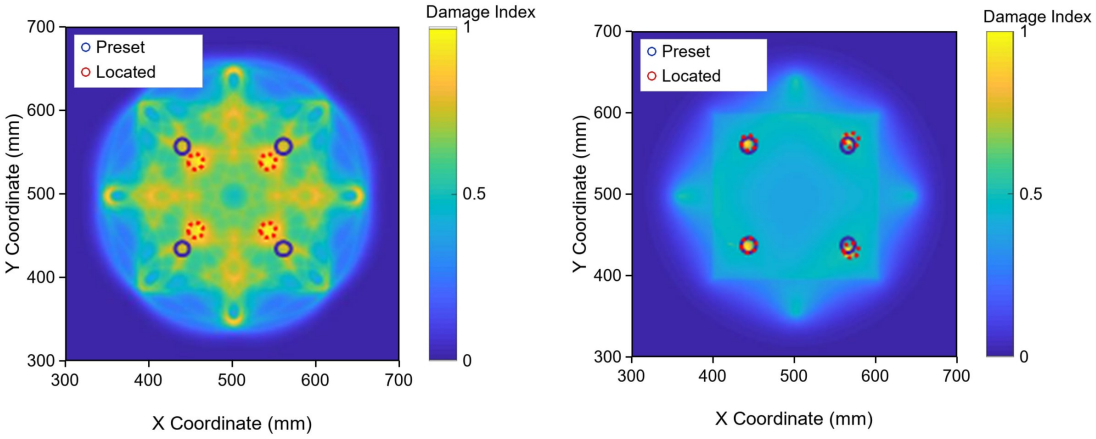


Figure 13. Four-defect simulation localization results. (**a**) Four-defect localization results of elliptic trajectory algorithm; (**b**) Four-defect localization results of PSO-based elliptic trajectory algorithm.

With four defects, the elliptic trajectory algorithm drifts further in both X and Y, while the PSO-based algorithm keeps a smaller positioning error. The positioning errors of the two methods are shown in Table 7.

Table 7. Four-defect simulation localization error table.

Algorithm Name	PSO-Based Elliptic Trajectory Algorithm	Elliptic Trajectory Algorithm
Preset Damage Coordinates	1.(435, 435), 2.(435, 565) 3.(565, 565), 4.(565, 435)	1.(435, 435), 2.(435, 565) 3.(565, 565), 4.(565, 435)
Algorithm-Localized Damage Coordinates	1.(431, 430), 2.(433, 567), 3.(570, 569), 4.(568, 431)	1.(456, 455), 2.(455, 543), 3.(543, 544), 4.(544, 456)
X and Y Coordinate Localization Error (mm)	1.(−4, −5), 2.(−2, 2), 3.(5, 4), 4.(3, −4)	1.(21, 20), 2.(20, −22), 3.(−22, −21), 4.(−21, 21)
Relative Distance (mm)	1.(6.40), 2.(2.83), 3.(6.40), 4.(5.00)	1.(29.00), 2.(29.73), 3.(30.41), 4.(29.70)
Localization Error ε_{loc}	1.(0.0221), 2.(0.0098), 3.(0.0221), 4.(0.0172)	1.(0.1000), 2.(0.1025), 3.(0.1049), 4.(0.1024)
Mean Error	0.0178	0.1025

Across the three damage conditions, the conventional algorithm was less accurate than the PSO-based one in every case, with mean errors of 0.0658, 0.1739 and 0.1025 for two, three and four defects; the error therefore did not grow monotonically with the number of defects, its maximum occurring in the three-defect case, whereas the PSO-based algorithm kept its mean error between 0.0093 and 0.0178.

A comparative analysis of the damage localization errors under the three damage conditions using the two methods is presented in Figure 14. Against the elliptic trajectory algorithm, the PSO-based algorithm keeps the mean error at or below 0.0178 in all three configurations (Tables 5–7).

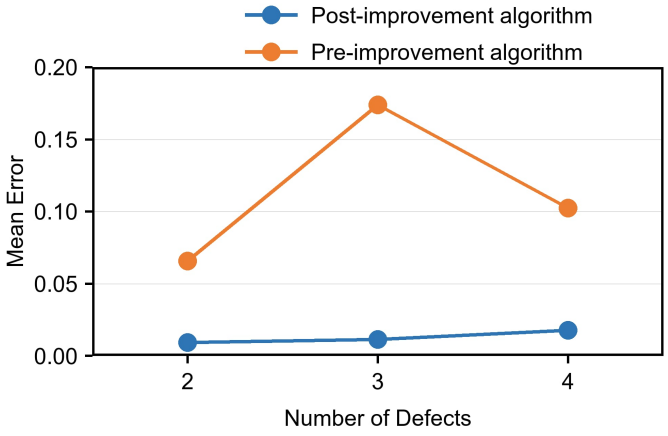


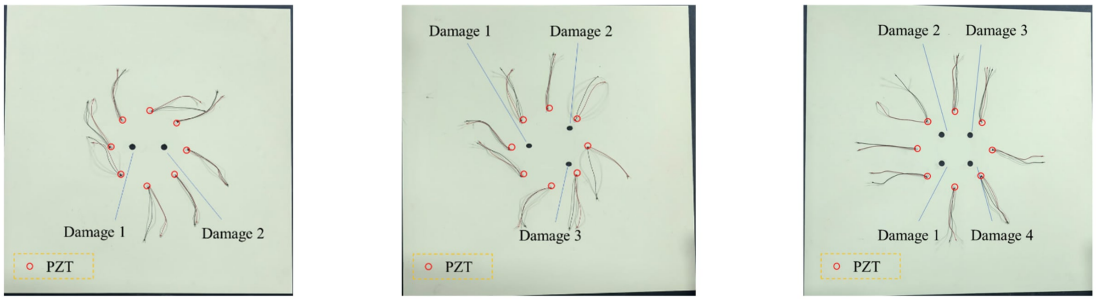
Figure 14. Simulated mean localization error of the conventional elliptic trajectory algorithm with empirical parameters and of the PSO-optimized algorithm.

Furthermore, by analyzing the guided-wave signals obtained under the three aforementioned preset damage conditions, it can be found that the influence of wave reflections between multiple defects is limited under the experimental conditions of this study. Specifically, the energy of single-scattered waves is well above that of multi-reflected waves between defects, and the wavelet transform and envelope peak extraction method adopted in this study mainly capture the dominant first-arrival scattered signals. Furthermore, the multi-path superposition and non-maximum suppression strategies can effectively suppress pseudo peaks caused by weak multi-reflected waves. As such, the interference of inter-defect wave reflections does not become the main source of localization error in this study.

3.2.2. Experimental Verification

(1) Experimental System Construction

To further verify the feasibility of the proposed method in practical engineering applications, a test experiment was conducted using a Q235 steel plate (treated with rust prevention) with the same dimensions and material properties as the simulation model. The same excitation method and PZT arrangement as those in the simulation were adopted in the experiment. The PZTs used in this test had a diameter of 8 mm and a thickness of 0.5 mm, and were bonded to the surface of the plate using quick-drying glue. The test specimen is shown in Figure 15. The experimental test system was composed of a function generator, a power amplifier, and an oscilloscope. The model of the function generator is a UNI-T/UTG2025A, the power amplifier is an Aigtek/ATA-2021B, and the oscilloscope is a Tektronix/3-SERIES. The experimental system is shown in Figure 16.



(**a**) Two-defect specimen (**b**) Three-defect specimen (**c**) Four-defect specimen

Figure 15. Steel plate specimen used in the experiments.

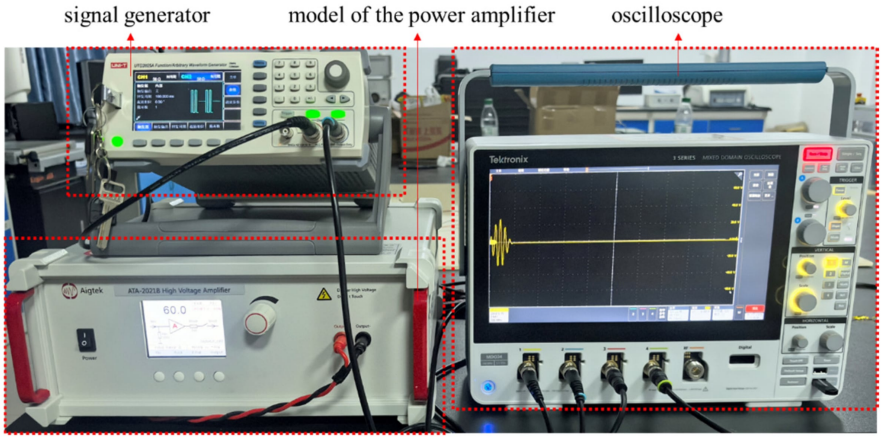


Figure 16. Experimental system.

(2) Guided-Wave Signal Processing

Due to the large number of guided-wave propagation paths involved in the test, this study only presents the complete signal processing flow of the 4th path (excited by piezoelectric sensor PZT1 and received by PZT5) under the two-defect case. The original guided-wave signal of this path is shown in Figure 17. Firstly, linear baseline correction was performed on the original signal to eliminate the baseline drift caused by sensor DC offset and signal linear drift (Figure 18); subsequently, Gaussian filtering was employed to denoise the signal after baseline correction, suppressing background random noise to improve the signal-to-noise ratio (SNR) (Figure 19).

It is known that the propagation distance between PZT1 and PZT5 is 290 mm. With the group velocities read from the dispersion curves of Figure 1 at the excitation frequency, the direct arrivals of this path are expected at 290/5.3 ≈ 55 μs for the S0 mode and at 290/3.2 ≈ 91 μs for the A0 mode. The signal that precedes any guided-wave arrival is attributed to the electrical cross-talk between the excitation and the receiving channel, a contribution common to all paths that is removed by the template subtraction of Section 2.3.1. These reference times fix the attribution of the packets in Figures 17–19: the first ≈85 μs of the record contain the electrical cross-talk between the excitation and the receiving channel together with the earliest part of the guided-wave response, the direct S0 arrival being expected at about 55 μs, and the scattering of the damage that lies on this path, which arrives at the same time as the direct modes and is therefore not separable from them in the raw record; the packet that appears around 250–340 μs is the component that remains once the healthy record is subtracted, i.e., the part of the response caused by the damage, which is separated in time from the direct modes and can therefore be extracted; and the packet that rises after about 380 μs is the boundary reflection received again by PZT5.

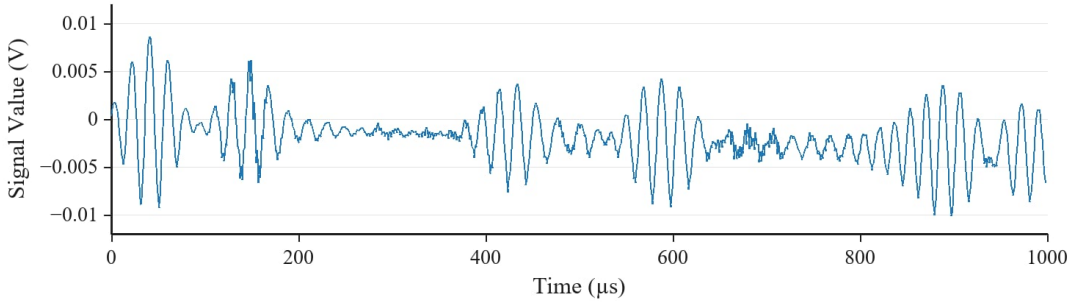


Figure 17. Original Lamb wave signal of the 4th path for the two-defect case.

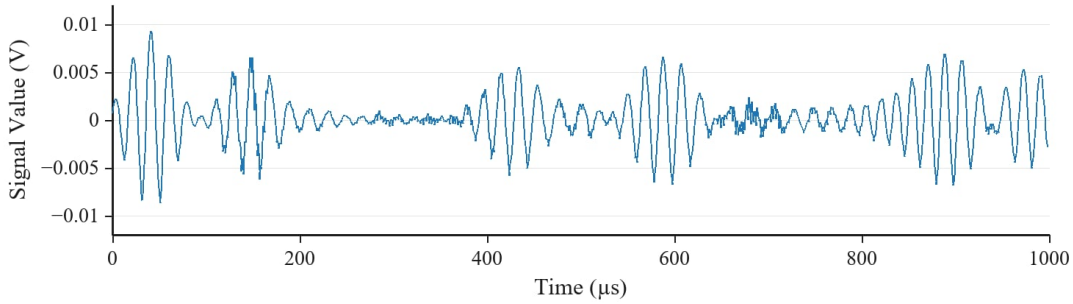


Figure 18. Lamb wave signal after baseline correction.

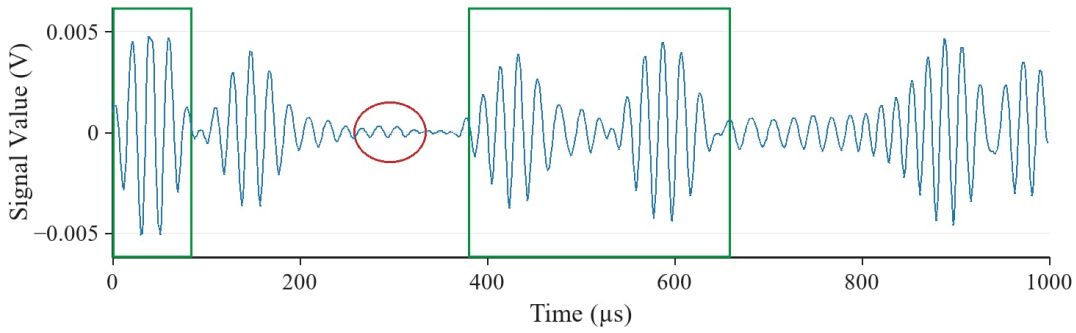
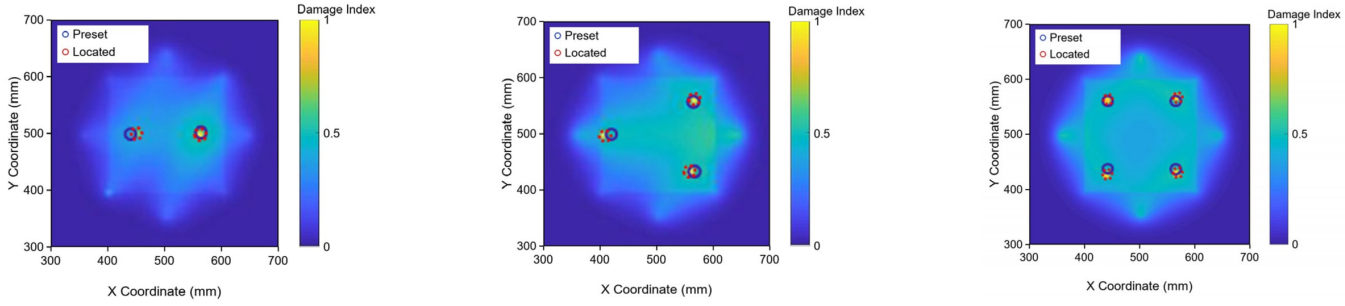


Figure 19. Lamb wave signal after Gaussian filtering.

(3) Damage Localization Result Analysis

After signal processing, the guided-wave data were imported into the PSO-based elliptic trajectory algorithm for damage position identification. The positioning results are shown in Figure 20.

The experimental accuracy in Figure 20 is slightly lower than in the simulations, and Figure 21 gives the corresponding error levels. The positioning errors are listed in Table 8. The mean errors obtained experimentally are 0.0146, 0.0237 and 0.0242 for the three configurations (Table 8).



(**a**) Two-defect localization results (**b**) Three-defect localization results (**c**) Four-defect localization results

Figure 20. Experimental localization results for the Q235 steel plates under the two-, three- and four-defect conditions.

The experimental localization error is slightly larger than the simulation result, and the main sources of error are summarized as follows: (1) The bonding error of PZT leads to the slight deviation of the actual sensor coordinates from the preset values, which affects the calculation of the elliptic trajectory; (2) The random environmental noise and the DC offset of the detection system introduce small interference to the guided-wave signal collection and processing; (3) The slight unevenness of the steel plate surface and the manual operation

error in the experiment cause the minor attenuation of guided-wave energy propagation. These effects are not compensated in the present implementation, and their combined influence is reflected in the difference between the simulated and the experimental errors reported above.

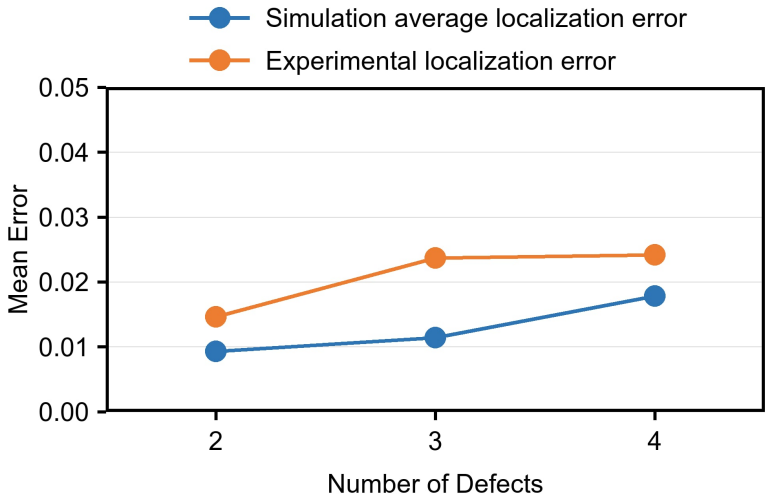


Figure 21. Simulated and experimental mean localization errors of the PSO-optimized algorithm.

Table 8. Experimental localization errors of the Q235 steel plates for the two-, three- and four-defect conditions.

Damage Conditions	Two-Defect Localization Results	Three-Defect Localization Results	Four-Defect Localization Results
Preset Damage Coordinates	1.(450, 500), 2.(550, 500)	1.(410, 500), 2.(545, 425), 3.(545, 575)	1.(435, 435), 2.(435, 565) 3.(565, 565), 4.(565, 435)
Algorithm-Localized Damage Coordinates	1.(457, 501), 2.(551, 501)	1.(399, 498), 2.(546, 427), 3.(538, 576.5)	1.(429, 424), 2.(435, 567) 3.(569, 568), 4.(568, 427)
X and Y Coordinate Localization Error (mm)	1.(7, 1), 2.(1, 1)	1.(−11, −2), 2.(1, 2), 3.(−7,1.5)	1.(−6, −11), 2.(0, 2), 3.(4, 3), 4.(3, −8)
Relative Distance (mm)	1.(7.07), 2.(1.41)	1.(11.18), 2.(2.24), 3.(7.16)	1.(12.53), 2.(2.00), 3.(5.00), 4.(8.54)
Localization Error εloc	1.(0.0244), 2.(0.0049)	1.(0.0386), 2.(0.0077), 3.(0.0247)	1.(0.0432), 2.(0.0069), 3.(0.0172), 4.(0.0294)
Mean Error	0.0146	0.0237	0.0242

A comparative analysis of simulation and experimental results shows that the PSO-based elliptic trajectory algorithm has consistent localization performance in both the ideal simulation environment and actual experimental conditions. The mean localization errors of the simulation are 0.0093, 0.0114 and 0.0178 for the two-, three- and four-defect configurations, and those of the experiment are 0.0146, 0.0237 and 0.0242; the experimental errors exceeds the simulated ones by 0.0053, 0.0123 and 0.0064 respectively, which indicates that the calibration transfers from the numerical model to the laboratory specimen without re-tuning. The mean error remains within 0.0242 across the three experimental configurations

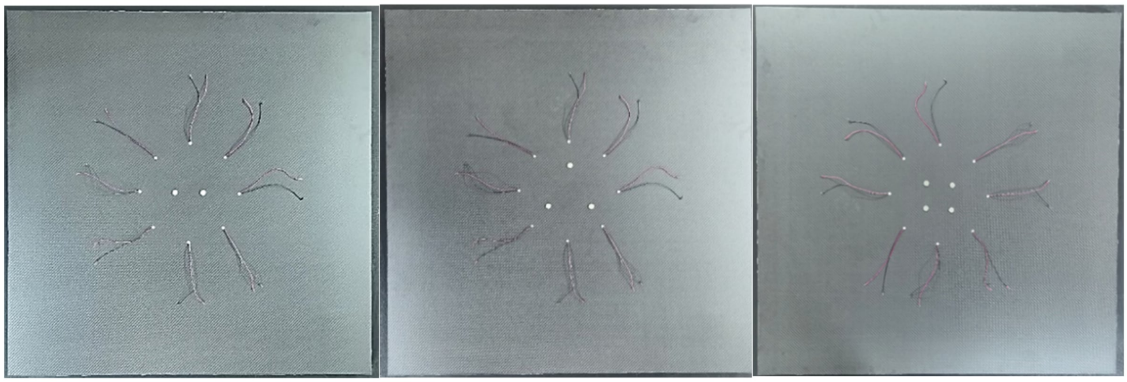
(Table 8); whether this level persists under varying temperature, coupling or noise level has not been tested (Section 4.2).

3.3. Damage Localization in CFRP Composite Laminates

This section applies the PSO-optimized elliptic trajectory algorithm to anisotropic composite materials. The CFRP part is validated experimentally only: modelling the laminate requires a layer-wise discretization whose homogenized properties could not be verified within the scope of this study, so the numerical study is restricted to the isotropic plate in Section 3.2. The CFRP specimens are 3K T700 woven-fabric laminates of 1000 mm × 1000 mm × 5 mm, the same material system as described in Section 2.1, and the PZT arrangement is the same as that for the steel plates.

3.3.1. Establishment of Composite Material Flat Plate Experimental Platform

To restore the real detection environment, a CFRP flat panel experimental platform was established with the same transducer array, excitation and acquisition chain as in the steel-plate experiments; the laminate was not modelled numerically, so the platform is matched to the steel experiments rather than to a simulation. The experimental test specimens were CFRP laminates with the same outer dimensions as the steel plates, 5 mm thick and with the layup defined in Section 2.1.2, as shown in Figure 22. The CFRP plates were loaded with magnets, which act as non-destructive simulated scatterers marking the damage sites; they are not intended to reproduce a through-thickness hole, and three damage scenarios identical to those in Section 3.1 were set up. The PZT piezoelectric sensors were fixed using quick-drying glue, and the sensor layout and path settings followed the simulation. The test system consisted of a function generator, a power amplifier, and a digital oscilloscope. The excitation signal parameters, sampling frequency, and signal conditioning method were all configured as in Section 3.1 to ensure that the experimental results were horizontally comparable to those of the steel plate experiments. The influence of the damage type and size on the localization accuracy is not investigated in this study, whose focus is the localization of multiple defects.

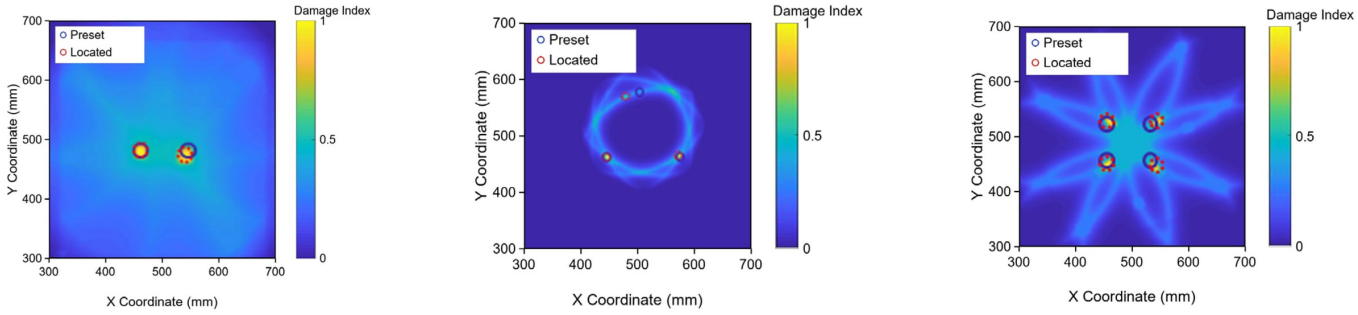


(**a**) Two-defect specimen (**b**) Three-defect specimen (**c**) Four-defect specimen

Figure 22. CFRP laminate specimen used in the experiments.

3.3.2. Damage Localization Result Analysis

The signal processing method for CFRP plates is the same as that for Q235 steel plates. The processed effective signals are input into the particle swarm optimization ellipse trajectory algorithm to complete the multi-damage localization calculation. The localization results are shown in Figure 23.



(**a**) Two-defect localization results (**b**) Three-defect localization results (**c**) Four-defect localization results

Figure 23. Experimental localization results for the CFRP laminates.

The experimental results show that, influenced by practical factors such as reflection at the composite interface and signal attenuation, the localization errors are larger than those obtained on the steel plates. For the CFRP specimens, the mean errors are 0.0098, 0.0416 and 0.0251 for the two-, three- and four-defect cases (Table 9); the three-defect case shows the largest error, which we attribute to the weaker scattered amplitude and the stronger attenuation in the composite rather than to the number of defects.

Table 9. Experimental localization errors of the CFRP laminates for the two-, three- and four-defect conditions.

Damage Conditions	Two-Defect Localization Results	Three-Defect Localization Results	Four-Defect Localization Results
Preset Damage Coordinates	1.(465, 500), 2.(535, 500)	1.(445, 455), 2.(555,455), 3.(500, 575)	1.(460, 460), 2.(460, 550) 3.(550, 550), 4.(550, 460)
Algorithm-Localized Damage Coordinates	1.(464, 501), 2.(532, 497)	1.(445, 455), 2.(552, 460), 3.(471, 566)	1.(459, 455), 2.(459, 554) 3.(557, 555), 4.(558, 452)
X and Y Coordinate Localization Error (mm)	1.(−1, 1), 2.(−3, −3)	1.(0, 0), 2.(−3, 5), 3.(−29, −9)	1.(−1, −5), 2.(−1, −4) 3.(7, 5), 4.(8, −8)
Relative Distance (mm)	1.(1.41), 2.(4.24)	1.(0.00), 2.(5.83), 3.(30.36)	1.(5.10), 2.(4.12) 3.(8.60), 4.(11.31)
Localization Error εloc	1.(0.0049), 2.(0.0146)	1.(0.0000), 2.(0.0201), 3.(0.1047)	1.(0.0176), 2.(0.0142) 3.(0.0297), 4.(0.0390)
Mean Error	0.0098	0.0416	0.0251

3.4. Cross-Material Localization Accuracy Comparison

To systematically evaluate the localization stability of the PSO-optimized elliptic trajectory algorithm across different material systems, this section compares the localization errors between Q235 homogeneous steel plates and CFRP composite laminates. The mean experimental localization errors of the two material types are summarized in Table 10 and Figure 24.

For the Q235 plates in Table 10, the mean experimental error is 0.0146, 0.0237 and 0.0242 for two, three and four defects: it rises slowly with the defect number, and each configuration was localized without a missed or false detection. For the CFRP plates, the mean experimental error was 0.0098, 0.0416 and 0.0251 for two, three and four defects, remaining at or below 0.0416 in all three configurations. In every configuration tested, each

preset defect produced an accepted peak, while no spurious peak passed the threshold. The statement covers the configurations examined here, not an arbitrary arrangement of defects.

Table 10. Comparison of positioning errors between Q235 plates and CFRP plates.

Material Properties	Mean Error (Two Defects)	Mean Error (Three Defects)	Mean Error (Four Defects)
Q235	0.0146	0.0237	0.0242
CFRP	0.0098	0.0416	0.0251

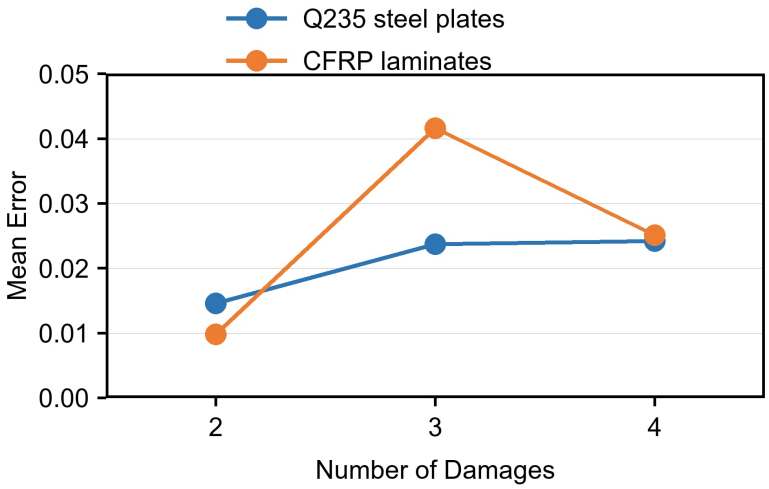


Figure 24. Experimental mean localization error for the two material systems.

The difference between the two materials depends on the damage configuration. With two defects, the laminate gave a lower mean error than the steel plate (0.0098 against 0.0146); with three defects, its error rose to 0.0416, against 0.0237 for steel; with four defects, the two were close (0.0251 and 0.0242). Localization accuracy therefore depends on both the material and the damage configuration, and the configurations tested here are too few to separate the two effects. The comparison is limited to the room-temperature, single-array case.

4. Conclusions and Future Work

4.1. Main Findings

This paper focuses on the issues of limited accuracy and empirical parameter dependence in traditional elliptic trajectory algorithms for multi-damage localization in plate-like structures, and proposes a PSO-optimized elliptic trajectory algorithm integrated with a pre-experiment global parameter calibration mechanism. The main findings are summarized as follows:

(1) A unified preprocessing and scattered-wave extraction framework is constructed for both isotropic metallic and anisotropic composite plates. Linear detrending and Gaussian filtering suppress the sensor DC offset, the acquisition drift and the background noise, while the subtraction of the one-off healthy-state template removes the direct arrivals and the excitation cross-talk; the A0-mode damage-scattered packets are thereby isolated, and their arrival times are picked without re-acquiring a baseline.

(2) The pre-experiment global parameter calibration mechanism can mitigate the subjectivity bias caused by manual parameter selection and the engineering difficulty of real-time parameter optimization for in-service structures. Taking the two-defect condition as the calibration benchmark, the PSO algorithm is adopted to adaptively

optimize three core parameters: ToF extraction threshold, equivalent group velocity and damage factor, and a single parameter set is obtained. Different from scenario-by-scenario parameter tuning, the calibrated parameter set can be uniformly applied to multi-damage scenarios with different quantities. This is what makes the set reusable across configurations.

(3) Verified by independent test sets, the proposed method achieves accurate localization on both material systems. Simulation results show that for Q235 steel plates, the mean localization errors of the two-defect calibration set, three-defect and four-defect independent test sets are 0.0093, 0.0114 and 0.0178. Experimental results indicate that the mean errors of the three conditions are 0.0146, 0.0237 and 0.0242 for Q235 steel plates, and 0.0098, 0.0416 and 0.0251 for CFRP laminates. A separate calibration was carried out for each material system on its two-defect configuration, and the resulting parameter set was then applied to the three- and four-defect configurations without re-tuning. The three sets differ most visibly in the equivalent group velocity, which follows the lower wave speed of the laminate, so what is compared across materials is the behavior of one procedure rather than a single parameter set transferred between materials.

In summary, the proposed method localized two to four defects with mean normalized errors between 0.0098 and 0.0416, that is, between 0.98% and 4.16% of the 290 mm aperture of the sensor array, without repeating the baseline acquisition during service. The pre-experiment calibration used non-destructive scatterers on the laminate and through-thickness holes on the steel plates, so a calibration that is entirely non-destructive is at present demonstrated for the laminate only. The same procedure may be useful for other guided-wave localization methods whose imaging parameters are at present chosen by experience.

Compared with the alternatives reviewed in Section 1, the present method asks least at the time of inspection. Probabilistic imaging needs a reference record, time reversal a transfer function of the pristine structure, and data-driven localization a labelled set covering the damage scenarios of interest. The ellipse-of-uncertainty approach instead quantifies how the ToF uncertainty propagates into the image, which is complementary to this work because the calibrated κ reduces that uncertainty at its source. Here, the requirement is one healthy record per structure and one calibration per material, with no labelled damage data.

4.2. Limitations and Future Work

Overall, the approach has three practical advantages. The parameters are calibrated once on a two-defect configuration and carried over unchanged to the three- and four-defect cases of the same material. The number of defects follows from the field itself through non-maximum suppression rather than being imposed. The position comes from the intersection of the loci rather than from the amplitude of the residual, so no amplitude calibration is needed.

The limitations are equally explicit.

(1) The forward model assumes single scattering between a defect and a sensing path and a single equivalent group velocity for all paths. Scattering between defects and the directional dependence of the group velocity are therefore not represented; the subtraction cannot remove the field that such scattering creates, the non-maximum suppression of Section 2.3.1 removes only peaks closer than the suppression radius to a stronger one, and a per-path velocity $C_g(\theta_k)$ would remove the second approximation at the cost of raising the PSO dimension from three to four or five.

(2) Defects must be separated by more than twice the suppression radius of 60 mm, so closely spaced defects are merged.

(3) Measurement noise, bonding error, surface unevenness and material inhomogeneity all displace the envelope crossing by a fraction of a sampling interval or a few millimeters over the 290 mm path. Their combined effect is bounded by the measured-minus-simulated errors of 0.0053, 0.0123 and 0.0064 and by the scatter of the ToF actually measured, but the contributions were not separated, and the noise level was not varied.

The two test series use different scatterers. The numerical model and the Q235 experiments use through-thickness holes, whereas the CFRP experiments use magnets bonded to the surface. They are of comparable size and strength but not identical, so the calibrated parameters are valid for scatterers of comparable strength. All defects lie on or close to a sensing path, where the ellipse degenerates into a segment and the localization is carried by the remaining paths; a defect far from every path is not covered and would require a separate campaign before extrapolation. Each configuration was measured in a single acquisition, so the mean errors of Tables 8–10 are not a statistical bound; repeated acquisitions can be provided.

The study is restricted to a flat 1000 × 1000 mm plate, one annular array of eight PZT sensors, one excitation frequency and one layup, at room temperature. Curved or stiffened structures, other arrays, other materials and other damage types would each require a new calibration. A per-path group velocity, coded or frequency-modulated excitation and a frequency-dependent description of attenuation are left for future work, the last for a dedicated study; multi-frequency fusion and data-driven localization would extend the method beyond the present scope.

Author Contributions: Conceptualization, S.T. and S.W.; Methodology, S.T., S.W. and Y.C.; Software, S.W., L.Z., Z.L. and Y.C.; Formal analysis, S.W.; Resources, S.T., S.W. and Y.C.; Data curation, S.W. All authors have read and agreed to the published version of the manuscript.

Funding: This work was supported by the National Natural Science Foundation of China (Grant Nos. 52475172 and 52275138) and the Key Science and Technology Research Project of the Henan Province (Grant No. 252102241039).

Data Availability Statement: The original contributions presented in this study are included in the article. Further inquiries can be directed to the corresponding author.

Conflicts of Interest: The authors declare no conflicts of interest.

References

1. Mitra, M.; Gopalakrishnan, S. Guided wave based structural health monitoring: A review. *Smart Mater. Struct.* **2016**, *25*, 053001. [CrossRef]
2. Farrar, C.R.; Worden, K. An introduction to structural health monitoring. *Philos. Trans. R. Soc. A* **2007**, *365*, 303–315. [CrossRef] [PubMed]
3. Aramburu, A.B.C.; da Cruz, J.A.; Xavier da Silva, A.A.; Acosta, A.P.; Minillo, L.Q.; de Avila Delucis, R. Non-destructive testing techniques for pressure vessels manufactured with polymer composite materials: A systematic review. *Measurement* **2025**, *246*, 116729. [CrossRef]
4. Yu, L.; Giurgiutiu, V. In situ 2-D piezoelectric wafer active sensors arrays for guided wave damage detection. *Ultrasonics* **2008**, *48*, 117–134. [CrossRef] [PubMed]
5. Yan, S.; Zhu, R.F.; Wang, X.N.; Chen, X.K. Damage imaging identification of plate structures based on linear array near-field MUSIC algorithm. *Nondestruct. Test. Eval.* **2025**, *40*, 3545–3577. [CrossRef]
6. Liu, X.Y.; Liu, Z.H.; Zhu, Y.P.; Lu, Z.J.; Chen, L.; Wu, B.; He, C.F. Multi-frequency instantaneous wavenumber damage imaging method based on ultrasonic guided waves induced by laser point-by-point excitation. *Nondestruct. Test. Eval.* **2025**, *40*, 2208–2224. [CrossRef]
7. Meng, L.; Guo, Z.; Ma, C. Research on multiple damage localisation based on fusion of the Lamb wave ellipse algorithm and RAPID algorithm. *Insight—Non-Destr. Test. Cond. Monit.* **2024**, *66*, 34–40. [CrossRef]
8. Kennedy, J.; Eberhart, R. Particle swarm optimization. In *Proceedings of ICNN'95—International Conference on Neural Networks*; IEEE: Perth, Australia, 1995; pp. 1942–1948. [CrossRef]

9. Shi, Y.; Eberhart, R. A modified particle swarm optimizer. In *Proceedings of the IEEE International Conference on Evolutionary Computation*; IEEE: Anchorage, AK, USA, 1998; pp. 69–73. [CrossRef]
10. Lomazzi, L.; Fabiano, S.; Parziale, M. On the explainability of convolutional neural networks processing ultrasonic guided waves for damage diagnosis. *Mech. Syst. Signal Process.* **2023**, *183*, 109642. [CrossRef]
11. Liu, G.; Wang, B.; Wang, L.; Yang, Y.; Wang, X. Probability-based diagnostic imaging with corrected weight distribution for damage detection of stiffened composite panel. *Struct. Health Monit.* **2022**, *21*, 1432–1446. [CrossRef]
12. Liu, Z.; Sun, K.; Song, G.; He, C.; Wu, B. Damage localization in aluminum plate with compact rectangular phased piezoelectric transducer array. *Mech. Syst. Signal Process.* **2016**, *70-71*, 625–636. [CrossRef]
13. Jin, H.; Wang, Y.; Sun, H.; Li, W.; Qing, X. Identification and imaging of multi-defects on a complicated composite structure by ultrasonic guided wave. *Polym. Test.* **2022**, *106*, 107466. [CrossRef]
14. Su, C.; Bian, H.; Jiang, M.; Zhang, F.; Sui, Q. Research on composites damage identification based on power spectral density and Lamb wave tomography technology in strong noise environment. *Compos. Struct.* **2022**, *289*, 115466. [CrossRef]
15. Chen, H.; Xu, K.; Liu, Z.; Ta, D. Ellipse of uncertainty based algorithm for quantitative evaluation of defect localization using Lamb waves. *Ultrasonics* **2022**, *125*, 106802. [CrossRef] [PubMed]
16. Tabjula, J.L.; Kanakambaran, S.; Kalyani, S.; Rajagopal, P.; Srinivasan, B. Outlier analysis for defect detection using sparse sampling in guided wave structural health monitoring. *Struct. Control Health Monit.* **2021**, *28*, e2690. [CrossRef]
17. Xu, C.; Yang, Z.; Qiao, B.; Chen, X. A parameter estimation based sparse representation approach for mode separation and dispersion compensation of Lamb waves in isotropic plate. *Smart Mater. Struct.* **2020**, *29*, 035020. [CrossRef]
18. Kannusamy, M.; Kapuria, S.; Sasmal, S. Accurate baseline-free damage localization in plates using refined Lamb wave time-reversal method. *Smart Mater. Struct.* **2020**, *29*, 055044. [CrossRef]
19. Kannusamy, M.; Kapuria, S.; Sasmal, S. An efficient Lamb wave-based virtual refined time-reversal method for damage localization in plates using broadband measurements. *Ultrasonics* **2022**, *124*, 106767. [CrossRef] [PubMed]
20. Xu, X.Q.; Tan, Z.W.; Hu, H.W.; Xiang, H.N. Research on Multi-damage Monitoring Method of Plate Structure Based on Guided Wave. *J. Mech. Eng.* **2025**, *61*, 130–141. [CrossRef]
21. Yuan, Q.; Kato, B.; Fan, K.Q.; Wang, Y. Phased array guided wave propagation in curved plates. *Mech. Syst. Signal Process.* **2023**, *185*, 109821. [CrossRef]
22. Ricci, F.; Monaco, E.; Boffa, N.D.; Maio, L.; Memmolo, V. Guided waves for structural health monitoring in composites: A review and implementation strategies. *Prog. Aerosp. Sci.* **2022**, *129*, 100790. [CrossRef]
23. Su, Z.; Ye, L.; Lu, Y. Guided Lamb waves for identification of damage in composite structures: A review. *J. Sound Vib.* **2006**, *295*, 753–780. [CrossRef]
24. Azad, M.M.; Munyaneza, O.; Jung, J.; Sohn, J.W.; Han, J.W.; Kim, H.S. Damage localization and severity assessment in composite structures using deep learning based on Lamb waves. *Sensors* **2024**, *24*, 8057. [CrossRef] [PubMed]
25. Liao, Y.; Qing, X.; Wang, Y.; Zhang, F. Damage localization for composite structure using guided wave signals with Gramian angular field image coding and convolutional neural networks. *Compos. Struct.* **2023**, *312*, 116871. [CrossRef]
26. Rautela, M.; Gopalakrishnan, S. Ultrasonic guided wave based structural damage detection and localization using model assisted convolutional and recurrent neural networks. *Expert Syst. Appl.* **2021**, *167*, 114189. [CrossRef]
27. Azimi, M.; Eslamlou, A.D.; Pekcan, G. Data-driven structural health monitoring and damage detection through deep learning: State-of-the-art review. *Sensors* **2020**, *20*, 2778. [CrossRef] [PubMed]
28. Tian, S.; Wang, S.; Chen, Z.; Hao, R.; Qin, Z.; Ma, J.; Xu, L. Damage Quantitative Detection of Curved Composite Laminates Based on Improved Particle Swarm Optimization Algorithm. *Materials* **2025**, *18*, 2317. [CrossRef] [PubMed]
29. Michaels, J.E. Detection, localization and characterization of damage in plates with an in situ array of spatially distributed ultrasonic sensors. *Smart Mater. Struct.* **2008**, *17*, 035035. [CrossRef]
30. Croxford, A.J.; Moll, J.; Wilcox, P.D.; Michaels, J.E. Efficient temperature compensation strategies for guided wave structural health monitoring. *Ultrasonics* **2010**, *50*, 517–528. [CrossRef] [PubMed]
31. Konstantinidis, G.; Drinkwater, B.W.; Wilcox, P.D. The temperature stability of guided wave structural health monitoring systems. *Smart Mater. Struct.* **2006**, *15*, 967–976. [CrossRef]
32. Moser, F.; Jacobs, L.J.; Qu, J. Modeling elastic wave propagation in waveguides with the finite element method. *NDT E Int.* **1999**, *32*, 225–234. [CrossRef]
33. Willberg, C.; Duczek, S.; Vivar-Perez, J.M.; Ahmad, Z.A.B. Simulation methods for guided wave-based structural health monitoring: A review. *Appl. Mech. Rev.* **2015**, *67*, 010803. [CrossRef]
34. Liu, W.; Liu, L.; Wan, Q.; Xiang, Y.; Xuan, F.Z. Baseline-free damage localization in multilayer metallic spherical shell structures using guided wave tomography. *NDT E Int.* **2024**, *147*, 103213. [CrossRef]
35. Zeng, L.; Lin, J.; Huang, L. A modified Lamb wave time-reversal method for health monitoring of composite structures. *Sensors* **2017**, *17*, 955. [CrossRef] [PubMed]

36. Yu, L.; Giurgiutiu, V. Multi-mode damage detection methods with piezoelectric wafer active sensors. *J. Intell. Mater. Syst. Struct.* **2009**, *20*, 1329–1341. [CrossRef]
37. Rose, J.L. *Ultrasonic Guided Waves in Solid Media*; Cambridge University Press: Cambridge, UK, 2014. [CrossRef]
38. Giurgiutiu, V. *Structural Health Monitoring with Piezoelectric Wafer Active Sensors*, 2nd ed.; Academic Press: Oxford, 2014. [CrossRef]

Disclaimer/Publisher's Note: The statements, opinions and data contained in all publications are solely those of the individual author(s) and contributor(s) and not of MDPI and/or the editor(s). MDPI and/or the editor(s) disclaim responsibility for any injury to people or property resulting from any ideas, methods, instructions or products referred to in the content.